Optimizing Image Fidelity with Heterogeneous Arrays

Thesis by

Stuartt A. Corder

In Partial Fulfillment of the Requirements
for the Degree of
Doctor of Philosophy

California Institute of Technology
Pasadena, California

2008
(Defended June 9, 2008)

.

List of Tables

List of Figures

w

Chapter 1

Simulations: Limitations of Dynamic Range and Image Fidelity

Abstract

We have conducted simulations to determine the impact of relaxing certain assumptions about the mosaicing process with interferometers including the impact of pointing errors, deviations from idealized primary beam shapes, inclusion of heterogeneous baselines, and large spatial scale recovery. We also explore the impact of source size, mosaic pattern sampling, and gain errors. We consider several source models including point-like and extended structures. We have determined that rms pointing of XX FRACTION OF A BEAM WIDTH results in a factor of X reduction in image fidelity over the perfectly pointed case. We find that gain error represents a GOOD?BAD proxy for pointing error.

OBVIOUSLY I PUT THE RESULTS IN HERE AS WELL AFTER I HAVE THEM ALL TOGETHER!! Finally we discuss the future of the simulations in the context of our current findings.

1.1 Introduction

While the concepts of and scientific motivation for high image fidelity and dynamic range imaging were provided in chapter **??**, there are several factors that damage fi-

---

Portions of this were published as Carma Memo 43 (Wright & Corder) delity and dynamic range. These detriments arise from random and systematic errors as well as inherent properties of the array used to collect the data (Cornwell, Holdaway & Uson, hereafter CHU). Theorectical arguements have been used to produce estimates of fidelity, but these estimates suffer from two, fundamental limitations. First, they assume antenna symmetry. Second, they treat antennas as uniform entities. In reality, symmetry breaking errors such as uncentered illumination pattern on the dish surface or ellipticity in the primary beam result in significant, systematic deviations from symmetry. In addition, such systematic deviations are rarely uniform across all elements resulting in a violation of the second assumption. The deviations between antennas result in decidedly different antenna performance and thus reduced fidelity in final image reconstruction.

Simulated observations can provide insight into which effects are truly ruinois and therefore require software or hardware intervention. Such simulations provide both quantitative measures of the decay of fidelity with various parameters for different models and qualitative represenations the changes in image appearance. However, to date, many difficult parameters have been simulated using proxies for various errors. Specificially, pointing and primary beam error have been simulated using gain error. Gain errors effect the fidelity by scaling the overall flux response and can provide a method of scattering the phase about the image. True pointing and primary beam error effect the image differentially, resulting in gradients across the illuminated sky relative to the assumed illumination. Given the degree of degradation of fidelity on the image is strongly dependent on the size and structure of the source (Mel's memo) it is ideal to provide individual estimates of the antenna based errors in the simulation.

We present a suite of simulations where we consider various models and sources of error. While these simulations are specific to CARMA, the methods are easily generalizable to any array. We focus on situations where fidelity and dynamic range are likely to be of concern. Our source models, discussed in section 2, are designed to span the range of typical, continuum observations. Simulations of spectral line observations, requiring that the beam be varied in size as a function of channel, are prohibitively time consuming to conduct in detail though are easily generalized from the simulations presented here. Typical errors, discussed in section 3, are addressed in terms of how they generally impact the data and are then applied to the simulations. Some of these variables have been simulated elsewhere but we present them here for completeness. We describe the simulations in detail in section 4. Our outcomes of the simluations are presented in section 5 while section 6 describes our conclusions and suggests further work providing a sample simulation of ALMA observations.

1.2 Models

To measure image fidelity, deviations from the known source properties must be measured. To ascertain the extent of damage to the fidelity and dynamic range on typical observations, a generalized suite of models which represent the typical science targets observered must be created. We generalize the typical observing targets into two groups, one composed of a distribution of compact sources and another a complex source with various levels of substructure. As a baseline we adopt a single, compact source model at the center of the telescope beam. This allows us to determine what impact the various models have on detection experiments. We also explore the effect of moving the point around in the center of the primary beam to determine what effect, if any this has on the derived properties.

MAKE FIG: LEFT PANEL LARGE IMAGE WITH LOTS OF SOURCES DISTRIBUTED OVER A LARGE REGION. WANT TO DISCUSS THE LIKELIHOOD OF ARTIFACT CREATION. RIGHT PANEL: COMPACT SOURCE WITH DISTRIBUTION OF BLOBS OVER A REALITIVELY SMALL AREA, DENSE. DEBRIS DISKS,

SECOND FIGURE: CASCVLA MODEL

Beyond our baseline model, we consider two general models with a few realizations each. The first general model, shown in Figure **??**, is a distribution of sources which are compact compared to the primary beam. In the left panel, 100 sources of various size and flux are distributed over the region of interest. The extent of the region is very large compared to the source size and the number density of sources per telescope primary beam is ≤1. Such a region is a good approximation to searches for star-forming cores or planet-forming disks in nearby molecular clouds. The right panel displays similar sources but now displayed over a much smaller area where the source separation is a significant fraction of the entire region and the density of the points per telescope primary beam is now >1. Such an image can represent confused regions such as those often seen in high mass star forming regions. We allow some of the sources in both models to be highly elliptical, simulating outflow like structures.

Figure **??** shows a Very Large Array (VLA) image of the supernova remnant CasA provides an example of a source which has at least some flux on scales similar to that of the primary beam. The size of the image relative to the primary beam will be altered. We explore cases where the image is contains flux on scales much larger than the primary beam of the largest telescope in the array to instances where the source fills only a fraction of the primary beam of the largest telescope. In addition to providing a model for supernova remenants, such a model is a good representation of of ABG stars, debris disks, planetary nebulea, and nearby galaxies.

1.3 Variables

There are a variety variables that can effect image fidelity. Here, we focus on these variables in the case of the heterogeneous CARMA and highlight the additional challenges inherent to the heterogeneous cases though in general the problems are usually present in homogeneous arrays to a similar extent. In cases were problems are exacerbated by heterogeneous arrays, it will be noted.

STRUCTURE HERE? KEEP IT CONSISTENT: 1) THE PROBLEM. 2) WHY IT IMPACTS 3) WHAT YOUR CHOICES ARE IN OBSERVING. (AT LEAST ONE FIGURE FOR (1) AND MAYBE MORE FOR (2)) DON'T TALK ABOUT SINGLE POINTING VS MOSAIC..THAT'LL BE COVERED LATER!!

1.3.1 UV-coverage and Recovery of Large Spatial Scales

The fundamental limitation on the image fidelity comes from the inherent properties of the interferometer in question. Interferometers only sample a finite portion of the Fourier transform of an image. The axes of the Fourier transform of the image are typically described in terms of spatial scales u and v and the Fourier transform sits on the uv-plane. The points at which measurements of the Fourier transform are known are known as the uv-coverage. To have dense uv-coverage means to have sampled significant fractions of the Fourier transform of the image.

While some information can be regained in the neighborhood of points measured in the uv-plane by recovery in the deconvolution process due to assumptions required about the source extent (Cornwell), direct recovery via inverting with respect to individual pointing centers (Ekers & Rots) or use of Cauchy relations in the complex plane, the interferometer cannot sample the flux distribution everywhere. This limiation is greatest in cases where there are few antennas in the array or large regions requiring multiple pointings are to be observed. In the former case, the number of baselines sampling the uv-plane is inherently sparse. In the later case, the size of the region impacts the sampling of the the uv-plane associated with individual patches of sky as the telescope cannot be on every piece of sky for the entire time. Arrays with large numbers of antennas can recover large fractions of the uv-plane but are still limited by the sampling of the central region of the uv-plane as the antennas cannot be placed arbitrarily close together. This region, however, is associated with the largest scales in the map and sets the limits on the integrated flux. Therefore, inherent limitations come from the inability to recover the flux on the largest spatial scales and the ability to sample other size scales sufficiently well. (WHAT DOES THAT MEAN EXCATLY.) A single dish telescope is required to recover the flux on the largest scales. Figure **??** illustrates the uv-coverage of CARMA using *only* the D configuration (left panel), D+E configurations (center panel) and D+E+10m single dish (right panel).

1.3.2 Gain Noise

:

The gain solution is required to calibrate source visibilities:

EQUATION

where blah is blah and blah is blahblah. The calibration of the gains is normally done by periodic observations of a point source.

If the calibration is in error, an amplitude selfcalibration to derive the antenna based gains will be in error. This error will transfer to the source visibilities as a systematic error. The impact is to scatter flux in the map.

Instrument stability and the variability of the weather set the fundamental limit to the gain stability. It is necessary to estimate the gain on time scales which can either track the weather over time, or sample the typical variation cycle in the weather and the instrument. The first case requires incredibly bright and/or near to source calibrators, typically not available in the millimeter, while the second can sacrifice significant source integration time for long baseline configurations. Given this, there is little to be done to allieviate the detrimental effects of gain noise, aside from that introduced by pointing error which is discussed below. However, gain noise helps to set the fundamental limit of the achievable image fidelity.

1.3.3 Phase Noise

Phase noise bec

1.3.4 Sampling Interval

For mosaiced observations, the spacing to adopt between pointing centers is an important consideration. Sampling theory for a homogeneous array indicates that the nyquist sampling interval for a two dimensional mosaic pattern is the FWHM/$\sqrt{3}$. Sampling more sparsely than this rate will result in potential aliasing of some of the information and this image degradation. In the case of heterogeneous arrays the case is not nearly so clear. The potential aliasing is likely mitigated somewhat by the presence of additional antennas with larger beams though to what extend likely depends on source structure.

The choice of sampling interval is largely driven by source characteristics and science goals. If fidelity is not a tremendous concern because the source is likely to be suffiently faint that the impact of aliased flux is small, a larger sampling interval may be choosen. A larger sampling interval allows the observations to cover a greater area though less uniformly than smaller intervals would. Telescope overhead is a consideration as well. Here, we will address only one concern, the degree of fidelity detriment seen as a function of pointing spacing for the various models.

1.3.5 Size

source dependent/user choice for mosaic size.

The size of a source can influence the image fidelity. The primary beams have less sensitivity (see **??** to flux located away from the center of the beam. The visibilities in these regions will not be recovered as well as inner parts of the beam.

Difficultes with source size can be eleviated to some extent by observing through multiple pointings. However, such mosaicing does not come without difficulties. Requirements of system characteristics must be stricter (see below). Also, less sensitivity is gained over the central regions as better recovery of source information at the image edges is gained by directly pointing at those regions allowing less time on source.

1.3.6 Pointing

correctable

MAYBE MAKE THE STUFF TWO FIGURES ONE HOMO AND ONE HETERO?

Figure **??** displays the voltage pattern resulting from two antennas and the combined primary beam pattern of the two, i.e. the pattern which illuminates the source on the sky. The top two rows show two antenna voltage patterns (left and center) and their combination with the upper row depicting a homogeneous baseline and the second row illustraiting the heterogeneous bsaeline. The lower rows show various levels of misalignment of the beams from pointing error.

The impact of pointing error on the image is three fold. First it excites a gradient relative to the nominal antenna pattern assumed in the deconvolution process. Figure **??** illustrates the problem. Here we have divided the offset pointing primary beam by the assumed model. In the case of perfect pointing where the image reconstruction and deconvolution process correctly assumes ideal pointing, these images would be one everywhere. However, even for the modest pointing error described here there is a resulting gradient across the image, i.e. assumed pointing and real pointing mismatch to the assignment of flux is in correct. Another way to see this is to simply realize that the visibilities are given by:

EQUANTION

The second error arrise from the ellipticity of the resulting beam, i.e. non-systematic pointing error. The fits to the resulting beams shown in Figure **??**, both heterogeneous and homogeneous, seem to harbor little ellipticity but resulting Gaussian fits to the beams reveal ellipticity present at the XX% level. Coupled with antennas with inherent ellipticity this may produce a significant impact on the resulting illumination pattern especially as the beam rotates on the sky. Finally, pointing error can induce gain error. Improper pointing on the phase calibrator, provided an amplitude selfcal is performed, can introduce amplitude and phase errors which in turn can reduce image fidelity.

The methods for dealing with pointing error are varied. A recent approach allows the antenna based offsets to be a free parameter and a minimization to be obtained (CITE). Another obvious approach is to simply limit the errors in the pointing at the time of observation. Indeed a combination of such approaches will likely yeild the best results as limiting input pointing error allows the convergence of minimations techniques to occur over much shorter time scales. In **??** we will discuss the methods implemented at CARMA to optimize the pointing performance.

1.3.7 Primary Beams

Figure **??** can also be used as a basis for discussing primary beam error effects. The width of the voltage pattern is determined to the greatest degree by the antenna aperture and focus. Typically the voltage pattern is given by the wavelength of observation over the antenna diameter, though typically, due to the under-illumination of the dish edges to reduce spill-over, the effective diameter is true beam is slightly larger than this nominal value. In practice the primary beams for antennas are assumed to be uniform from telescope to telescope, entirely real, and circularly symmetric. Beams in the millimeter are also typically truncated at the 5% level, though for truly high dynamic range cases, side-lobe and wing contributions from the beam may impact the data.

In reality the assumptions of uniformity, realness and symmetry are all violated to varying degrees and the beam shape beneath the 5% truncation level can be significant. In the heterogeneous case, on which we will focus here, these are particularly damaging. Deviations from the nominal voltage pattern are typically reduced by the fact that small voltage response in the one antenna is multiplied by small voltage response in another antenna. In the heterogeneous case, this is simply not true. Specifically for CARMA, the 10% point of the 10m voltage pattern which would normally be multiplied by another 10% point, is multiplied by the Y% point of a 6m antenna instead. In the case of the soon to be added SZA antennas, the 10% point would then be multiplied by the Z% point. Here, deviations at these lower levels are not mitigated in creation of primary beam patterns and deviations from the nominal beam model and/or the shape of the beam beyond the 5% point can become significant.

Figure **??** shows possible deviations from the optimal antenna voltage pattern. Antenna astigmatism, often induced by gravitational forces and many vary as a function of elevation, often causes voltage pattern ellipticity. The top row shows a beam of 5% ellipticity on the left and the same beam divided by a standard voltage model on the right. With this, circular symmetry is violated. The bottom row shows the similar case for a focus error, which would produce a larger than expected beam. In the case of CARMA, these deviations, when present in the 10m antennas, are not reduced in formation of the primary beam. To further complicate the issue, it is unlikely that focus error will be uniform across all telescopes and that the degree and axis of ellipticity will be a constant resulting in an entire ensemble of voltage patterns, breaking the assumption of uniformity. Higher order phase structure in the dish results in XXXXXXXX in the voltage pattern. Imperfect alignment of the antenna optics can result in a phase gradient across the beam on the sky, violating the assumption of a perfectly real beam. In the end, even if perfect surface adjustment and alignment were possible, these optimizations need to be done at specific elevations and thus problem will still arise. Finally, small misalignments in the panels can produce amplitude structure in the volage pattern, scattering power into sidelobes and corrupting the main beam shape.

There is little choice to solve the problems. Like the case for pointing, we must appeal to either iterative processes to determine the true beam shape or models of the beams must be provided so that the proper source illumination can be utilized. It is our belief that the beams should be optimized to as great an extent as possible via panel adjustment and optical alignment and then models provided for the beams using astronomical measurements. Again, optimization techniques could be used but with proper models in place the convergence timescale would be greatly reduced.

1.4 Simulations & Metrics

points: size, flux, position, artifacts points large models: deviations from the fundamental image

1.5 Results

1.5.1 models..

1.6 Conclusions

watch out for pol and mosaics!

Bibliography

Chapter 2

Holography

Abstract

Modest and low-resolution holographic measurements of the 15 antennas of the Combined Array for Research in Millimeter Astronomy (CARMA) were made to determine the voltage patterns, antenna illumination patterns and large scale surface errors. Resolutions of ≥0.71 m and ≥0.42 m in the aperture plane amplitude and phase pattern were obtained on the 10.4 m and 6.1 m, respectively. Early measurements showed that the dominant source of error for the 10.4 m antennas was misalignment of the optical surfaces while the errors in the telescope surfaces dominated the 6.1 m data. Optical alignment of the 10.4 m antennas was performed at 3 mm, reducing the 3 mm alignment errors from as much as 1 m to <0.5 m. Surface RMS values of the antennas, which were initially distributed between 110 μm to 25 μm, are now between 37 and 23 μm. After the corrections were performed, holographic measurements were then done to determine the actual shape and stability of the voltage patterns on the sky. The width of the default Gaussians used by MIRIAD need to be altered as the model 6.1 m and heterogeneous baseline primary beams are too wide compared with measurement. The measured voltage patterns are consistent with Gaussian profiles down to the 10% level but are considerably narrower below. At the 5% cutoff points,

---

Portions of this chapter were previously presented in Carma Memos 36 (Corder & Wright) and 45 (not done yet..Corder & Wright).

Active focus correction and subsequent alignment of the optics will require a re-assessment of the voltage pattern properties described here. Alignment, especially at 1mm, will likely yield substantially different voltage patterns.

the profiles can differ by as much as 7”. The 6.1 m antennas have ∼4% ellipticity on the average though the various antennas have ellipticity varying from ≤3% to 6%. There is consistent evidence of phase gradients across several voltage patterns, especially on the 10.4 m antennas, which dominates the ellipticity in the amplitude voltage pattern. Side-lobes of as much as 15% were found for the 10.4 m antennas though maximum values of 10% are more typical. These sidelobe patterns are consistent from run to run at the 20% level. Finally antenna specific voltage patterns are provided for use when extra image fidelity it needed.

2.1 Introduction

The Combined Array for Research in Millimeter-wave Astronomy (CARMA) is currently composed of the six 10.4 m (C1–C6) antennas of the Owens Valley Radio Observatory (OVRO) millimeter array and the nine 6.1 m (C7–C15) antennas of Berkeley-Illinois-Maryland Array (BIMA). Since transporting the antennas to their current location at Cedar Flat subjected the them to a range of unusual stresses, it was critical to verify their optical and receiver alignment and the antenna illumination and surface shape. Deviations in illumination pattern and large scale surface errors result in poorer than expected signal to noise and incorrect primary beam deconvolution from mosaiced images. The goal of holography is to increase the aperture efficiency of the antenna while optimizing and/or determining precisely its voltage pattern.

The voltage pattern is the shape of the response of an individual antenna to emission on the sky. To measure deviations from the ideal illumination and shape of the antenna surface, I must measure the shape of this voltage pattern on the sky. The relationship between the voltage pattern in the sky plane and the illumination pattern in the aperture plane is a Fourier transform:

$$V_p(\vec{u}) = \frac{1}{\sqrt{2\pi}} \int_{\infty}^{\infty} A(\vec{k}) e^{2\pi\vec{k}\vec{u}} d\vec{k} \tag{2.1}$$

where V_p is the voltage pattern on the sky and A is the distribution of voltage in the aperture plane. The distribution A is typically a Gaussian, tapered so that it is small at the edge of the aperture to reduce spill-over. The voltage pattern is related to the more typically used *primary beam* by:

$$PB = V_{p1} \times V_{p2}^{*} \tag{2.2}$$

where the voltage pattern is as defined above and the second voltage pattern is conjugated. For strictly real, circularly-symmetric, Gaussian voltage patterns, the primary beam is a Gaussian of width a factor of $\sqrt{2}$ smaller than the voltage pattern, given by the standard relationship $FWHM = \epsilon\frac{\lambda}{D}$ where $FWHM$ is the full-width at half maximum, λ is the observing wavelength, D is the telescope diameter, and ϵ is a factor of order unity which depends on the taper.

In its most general form, the voltage patterns are complex leading to a primary beam of form:

$$\begin{aligned} PB_{mn}(\vec{u}) &= V_m(\vec{u})V_n(\vec{u})^{*} \\ &= (Re(V_m) + iIm(V_m))(Re(V_n) - iIm(V_n)) \\ &= (Re(V_m)Re(V_n) + Im(V_m)Im(V_n) + i(Re(V_n)Im(V_m) - Re(V_m)Im(V_n)) \end{aligned}$$

with the resulting amplitude and phase:

$$|PB_{mn}| = (Re(V_m)^2 + Im(V_m)^2)(Re(V_n)^2 + Im(V_n)^2)^{0.5} \tag{2.3}$$

$$\theta(\vec{u}) = tan^{-1}(\frac{(Re(V_n)Im(V_m) - Re(V_m)Im(V_n)}{Re(V_m)Re(V_n) + Im(V_m)Im(V_n))}) \tag{2.4}$$

For modest resolution holography (~1 m or better), the expected aperture illumination is a broken ring with a depression in the center and a Gaussian taper toward the edges. The central depression is due to subreflector blockage while the breaks in the ring are due to the secondary support legs. There are three and four legs on the 6m and 10m antennas, respectively. Ideally the general pattern should be as symmetric as possible and well centered. The phase across the aperture should be zero. Lower resolution holography, where the secondary is not resolved, generates a Gaussian illumination pattern without breaks or central depressions. High resolution holography, not presented here, generally shows depressions at the panel edges due to small gaps at the panel joints. Ideally, on the sky, the core of the real part of the voltage pattern should have a near Gaussian shape and there should be no contribution from the imaginary part. The locations of the sidelobes are not well known from observations.

Bulk deviations from ideal voltage pattern or aperture illumination and phase have easily calculable implications. Mispointed observations on the sky result in an offset of the voltage pattern from the expected location. A quick application of the Fourier Transform Shift Theorem:

$$\mathcal{F}^{-1}V(\vec{u}-\vec{u}_0)(\vec{x}) = e^{2\pi\ i\vec{x}\vec{u}_0}A(\vec{x}) \tag{2.5}$$

$$\mathcal{F}A(\vec{x}-\vec{x}_0)(\vec{u}) = e^{-2\pi\ i\vec{u}\vec{x}_0}V(\vec{u}) \tag{2.6}$$

shows that a shift in $\vec{u}$ (on sky) causes a phase gradient in the aperture plane. Similarly, misalignment of the antenna optics can give an offset of the illumination pattern in the aperture plane which results in a phase gradient across the voltage pattern on the sky, i.e. the imaginary voltage pattern becomes non-zero. Peak-up observations can easily rectify pointing offsets but more complicated optical alignment is necessary to center the illumination pattern. Figure 2.1 shows an concrete example of the impact of offset illumination patterns in the aperture plane. An offset of less than $\frac{1}{20}^{th}$ of a antenna diameter can result in a 15% peak contribution to the imaginary voltage pattern. This results in phase which ranges between ±20° from half power point to half point of the real voltage pattern.

Additional bulk deviations are possible. Principle axis (towards/away from the antenna surface) focus errors result in phase errors in the aperture plane. The magnitude of the phase error grows as a function of the square of the distance to the

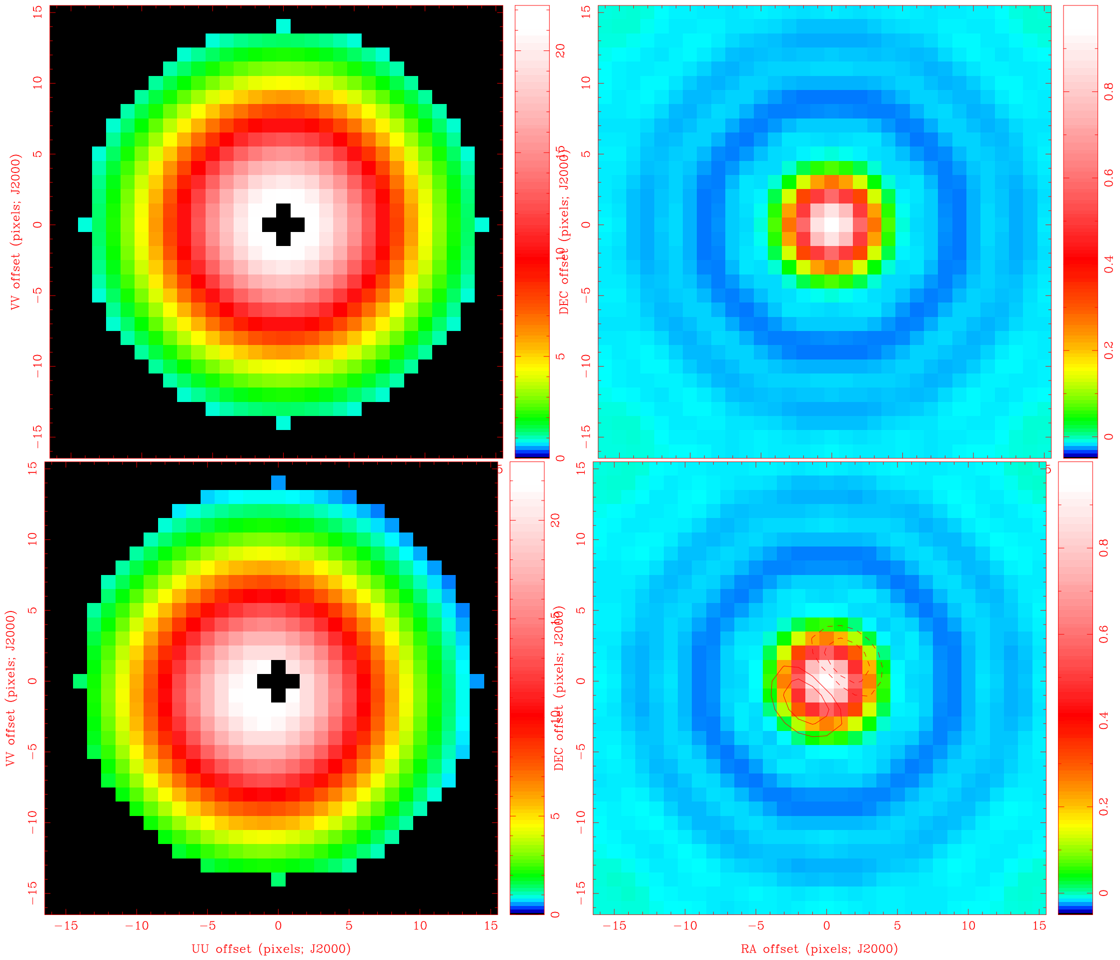

Figure 2.1 The left column shows a model of the aperture plane in the limit of a perfect surface, i.e. no phase contribution and perfect alignment. The depression in the middle of the amplitude pattern is from obstruction by the secondary. The right column is the sky plane with real component in color and normalized to 1 and the imaginary part shown as contours. Dashed contours are negative contributions. Contours are ±5% and 10% with dashed negative contours and solid positive contours. The aperture plane illumination is offset by 1 pixel in each direction, an offset comparable to 0.5 m on a 10.4 m telescope or 0.3 m for a 6.1 m telescope.

center of the antenna, a consequence of the parabolic shape of the dish. This unfortunately results in a widening of the voltage pattern on the sky *and* the excitation of an imaginary contribution. Focus corrections can be made by fitting a quadratic function to the aperture plane phase. Higher order corrections typically result in alternating phase around the surface of the dish. For example, astigmatism, resulting from an antenna surface which is compressed in one direction, has a surface phase pattern where the axis of the compression has one phase sign and the opposite phase sign perpendicular to the axis. Localized panel misalignment will appear as a single deviant region, not a systematic pattern.

I carried out a series of moderate-resolution holography measurements over the course of the spring and summer of 2006 and further, moderate- to low-resolution measurements in the fall of 2007 to the spring of 2008. Here, *modest* resolution implies 14-20 resolution elements across the dish surface while *low* resolution comprises only 6-10 such resolution elements. The goal of the first round of holography was to optimize the dish surface and align the optics. The second run was intended to measure the stability of the voltage patterns, determine their true shape including departures from a Gaussian profile and circular symmetry, and determine what, if any, antenna specific properties exist for the various antennas.

In §2.2, I discuss the data acquisition and reduction methods in general along with the datasets used to derive the relevant properties. In §2.3, I address the derived optical axis offsets and the values post correction, the preliminary measurements of 1mm optical alignment and the derived panel adjustment and the RMS after the correction. In §**??**, I turn to voltage patterns, measuring the accuracy of the currently used Gaussian models of the primary beams at CARMA, determining the departures from Gaussian profiles and/or circular symmetry, and finally discuss antenna specific voltage patterns for use when extreme image fidelity is required. I review the principle conclusions and summarize the work in §**??**.

2.2 Data Acquisition and Reduction

Voltage patterns of the 15 CARMA antennas were obtained using a bright point source and the CARMA beam-mapping software utility **multiMap** (White & Corder, 2007). Initial pointing corrections were obtained on the target itself utilizing the CARMA real-time radio pointing software utility **refPoint** (White & Corder, 2007). When obtaining voltage pattern data for the 10m antennas, the 6m antennas were held fixed for gain reference while the 10m antennas moved to a list of prescribed azimuth and elevation offsets. Conversely, while data was being obtained for the 6m antennas, the 10m antennas served as reference.

The offset positions were given as 90% of the Nyquist sampling interval for the moving antennas. The offsets were required to lie within a fixed circular radius to provide uniform resolution in the aperture plane and reduce the number of points to be observed. Measurements at the center position were obtained at the beginning and end of the scan for each row and at every seven points within the row for rows larger than 8 points. Taking overheads into account, this provides a calibration measurement at offset position (0,0) every 2 minutes or less.

Given the constant upgrading and testing of the antennas during the period of these observations at Cedar Flat, the holography datasets never included all 15 antennas at any one time and the number of reference antennas available for verification of repeatability differs from dataset to dataset. I therefore rely on a compilation of different datasets to cover all antennas. Typically, each 10.4 m antenna used 5 to 6 reference antennas and each 6.1 m antenna used 3 to 4 reference antennas. I also note that there are inevitable variations in the data quality because some antennas were not available on days with the best observing conditions. Table 2.1 contains specific information on the various datasets.

Calibration and holographic imaging of the antenna surfaces used MIRIAD (Sault, Teuben, & Wright, 1995). Each dataset was split into separate 500 MHz frequency bands for both LO sidebands before self calibration. I separated the central pointing by replacing the u and v coordinates with azimuth and elevation offsets from the center, (Δaz,Δel). The central pointings were then identified for use in calibration by selecting (Δaz, Δel) = (0,0) using MIRIAD's **select=uvnrange**. For each antenna, the resulting calibrated voltage patterns for each reference antenna and frequency band were converted to real and imaginary parts, Fourier transformed from the sky plane to the aperture plane using the MIRIAD **fft** function, and masked to exclude any information arising from outside the aperture using the **maths** function in MIRIAD.

Table 2.1. Holography Data

Date	Size arcsec	Step arcsec	Soruce	Frequency GHz	Elevation degrees	Antennas
2006-May-10	517/882	27.23/46.42	3c273	88.5	50/35	1,2,4-6/7-15
2006-May-23	517/882	27.23/46.42	3c273	88.5	51/51	1,2,4,5/8-15
2006-May-30	517/882	27.23/46.42	3c273	88.5	44/52	1,2,4-6/7-9,11-15
2006-Jun-12	517/882	27.23/46.42	3c273	88.5	52/52	1,2,4,6/8-10,12,14,15
2006-Jun-22	517/882	27.23/46.42	3c279	88.5	45/43	1,4/7-15
2006-Dec-07	na/908	na/43.25	3c273	95.0	na/47	na/7,9,10,12-15
2007-Aug-12	541/na	25.74/na	Mars	105.8	57/na	1,2,5/na
2007-Sep-07	541/na	26.25/na	Mars	100.2	47/na	1-4/na
2007-Sep-09	na/940	na/44.75	Mars	100.2	59/na	na/7-14
2007-Sep-11	187/312	14.40/24.00	Mars	100.2	55-66/59-71	1-3,5,6/8-14
2007-Sep-11	187/312	14.40/24.00	Mars	100.2	75-68/73-61	1-6/7-14
2007-Sep-16	187/312	14.40/24.00	3c454.3	100.2	65/68	1,3-5/9-14
2007-Sep-16	86/na	6.60/na	3c454.3	227.3	64/na	3,4,6/na
2007-Sep-16	86/na	6.60/na	3c454.3	227.3	64/na	3,4,6/na
2007-Nov-09	187/312	14.40/24.00	3c454.3	100.2	61/57	1-4,6/7-15
2008-Feb-28	187/312	26.25/44.75	3c273	100.2	54/53	2,3,6/7,10,12-15
2008-Mar-21	84/na	6.46/na	3c273	227.2	42/na	1-6/na
2008-Mar-24	535/na	28.18/na	3c273	98.4	54/na	2-6/na
2008-Mar-27	535/na	28.18/na	3c273	98.4	44/na	2-6/na
2008-Mar-27	159/na	12.26/na	3c273	227.2	34/na	2-6/na

Note. — Values which contain a '/' are for 10.4 and 6.1 m antennas respectively. All tracks taken post-adjustment were done at night with the exception of the Mars tracks which sometimes continued slightly through sunrise. C15 & C8 had significant pointing error in August and September of 2007 and much of that data has been edited. C7 had persistent trouble with phase jumps that rendered most of the imaginary beam information useless upon further inspection. C2 had poor sensitivity until very recently and resulted in poor data quality in the wings of the beam. C6 was out of the array for cryogenic work in much of September and August 2007. The 2007-Sep-16, 1mm dataset is suspect for all antennas because there is enhanced phase noise due to the extended nature of the configuration used.

For the modest-resolution holography, the measurements result in amplitude and phase in the aperture plane with a typical resolution of 0.71 m and 0.42 m for 10.4 m and 6.1 m antennas, respectively.

The individual aperture images for phase were then fit using the MIRIAD task **imhol**. Imhol fits a function to the aperture phase accounting for the size of the secondary, removes principal-axis focus and pointing errors, and provides a new image data set with these errors removed. Imhol also calculates an RMS surface error from the phase information, in microns, both before and after the phase function fit, as well as an illumination-weighted, post-fit RMS surface error. The illumination weighted, post-fit RMS is typically used as it down-weights phase errors which come from regions of poor sensitivity and therefore are uncertain. The pointing and focus error subtracted images and fits were examined to verify that the solutions and residuals were consistent across frequency bands, upper and lower sideband of the LO, and reference antennas. A single, average image was then created. This averaging was done in the aperture plane to minimize the effects of the differing frequencies in each band.

To determine the orientation of the resulting images a piece of Mylar was placed on one 6.1 m and one 10.4 m antenna. The Mylar, possessing an index of refraction greater than 1, induces a phase lag for incident radiation that appears, in the aperture plane, as a depression in the antenna surface. For the 6.1 m antennas the aperture images need to be flipped top to bottom. For the 10.4 m antennas the baseline order is reversed resulting in an apparent *raised* surface and images flipped left to right compared to reality.

2.3 Holography Results: Alignment and Panel Adjustment

In general, optical alignment was necessary for the 10m antennas and surface panel adjustment was required for the 6m antennas. Deviations from ideal alignment and surface RMS values were measured for every antenna and are reported here although many were unaltered. Unaltered antennas provide an estimate of the typical repeatability and noise level of the various images.

For high image fidelity, especially for mosaicing, the RMS surface error of the antennas, after the removal of pointing and focus errors, should be $\sim 1\ over 40^{th}$ of the observing wavelength (Cornwell, Holdaway, & Uson, 1993). Therefore, for 1.3 mm observations, the target RMS surface accuracy is 30μm. In what follows 30 um is referred to as the surface accuracy benchmark. For optical alignment, the desired accuracy is best expressed as the contribution to the imaginary or phase voltage pattern (c.f. Figure 2.1 and equation 2.6). If this imaginary component represents less than 5% of the peak flux at the half-power point of the voltage pattern, the resulting contribution is negligible in cases were a dynamic range of less than about 250 is required. In what follows, the 5% of the peak flux at the half-power point of the voltage pattern is referred to as the alignment benchmark.

2.3.1 Optical Alignment

When determining optical alignment, measurement of the offset direction and magnitude is made more difficult because the most sensitive portion of the feed is obstructed by the secondary. As the offset increases, a simple centroid of the illumination pattern on the antenna surface grows more slowly as the most sensitive portions of the feed are exposed to the antenna surface. To further complicate the measurement, the truncation of the illumination pattern at the edge of the antenna further causes an underestimate of the offset. In principle the feedlegs also cause differences, but the width of these features is much smaller than a resolution element, making the blockage only fractional.

To determine the offsets I measure the centroid of the illumination pattern on the dish and then apply a derived correction term. The correction was determined by simulating various offsets and measuring the apparent centroid. Figure 2.2 shows two realizations of the model run, one each for a large (top, left) and small (top, right) offset. The correction factor as a function of measured offset is shown on the bottom. These measurements are intended to be approximate and were not used in the actual adjustment of the optics. The correction is 12-13% and is flat for offsets less than 15% of the antenna radius. Beyond 15% of the dish radius, the correction grows rapidly as dish edge effects begin to dominate, reaching more than 50% when the illumination is centered on the dish edge. The correction factor is similar for the 10.4 and 6.1 m antennas because the ratio of the obstruction/hole to the dish size is the same in both cases.

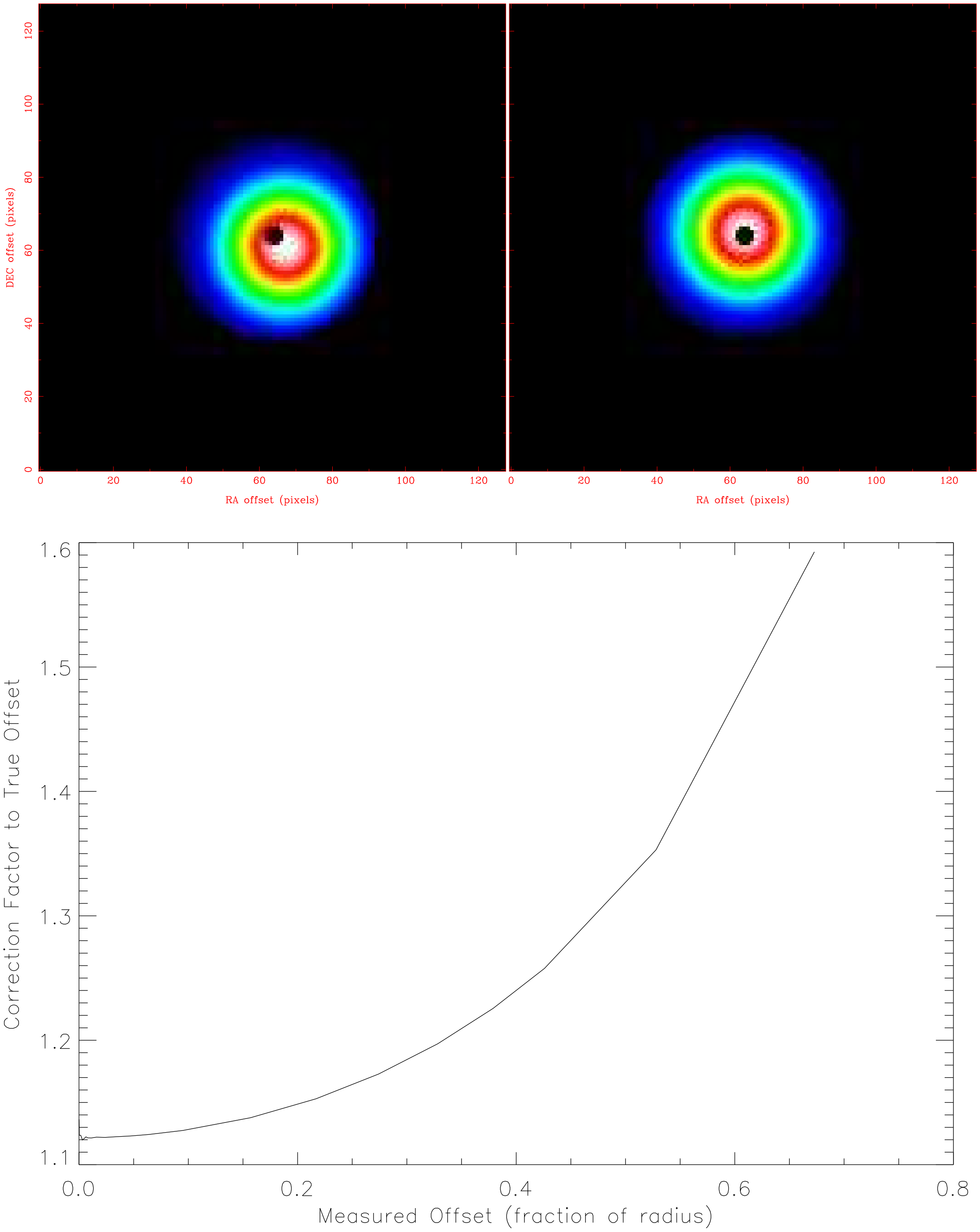

Figure 2.2 Top: The left and right panels show models of the dish surface illuminated by significantly offset (15% of the dish radius) and slightly offset (3.5% of the dish radius) illumination patterns. The lower panel shows the correction factor that needs to be applied to a given measured centroid to determine the actual offset in the aperture plane. For measured offsets less than 15% of the dish radius, the correction factor is a relatively constant 12.5±0.5%. Between 15 and 20% offsets the dominate effect changes from obstruction by the secondary to truncation at the dish edge. The correction factor goes quickly to zero for vanishingly small offsets. Discrete pixel sizes, which are present in the actual datasets, yield the apparent, unsmooth behavior at

Actual adjustment of the optical alignment for the 10.4 m antennas was carried out by placing a bright incoherent illumination source at the center of the secondary and aligning the mirrors and receiver so the optical beam tracks through the center of the four mirrors in the 10m system reaching a focus on the center of the feedhorn (Woody, 2008). There are no points at which the 6m system can be easily aligned making misalignment a serious problem if it occurs (Plambeck, 2008). The alignment of the optics can change if the receiver is removed from the dewar and is replaced with a different setting.

Figure 2.3, depicting C4, shows an example of 10m alignment. The left panel is pre-adjustment data taken on 2006 May 10 while the right panel shows post-adjustment results for 2006 June 12. In the left panel the alignment is significantly deviant from the nominal position. The pattern appears to be offset by 1 m at an angle of 24° counterclockwise from up. Following adjustment the offset was 26° clockwise from up and is offset by 0.46m. Holography carried out in 2007 September indicates that the magnitude and direction of this offset have remained to within 15% in magnitude and 20°, respectively, suggesting that the alignment offset persists over long timescales.

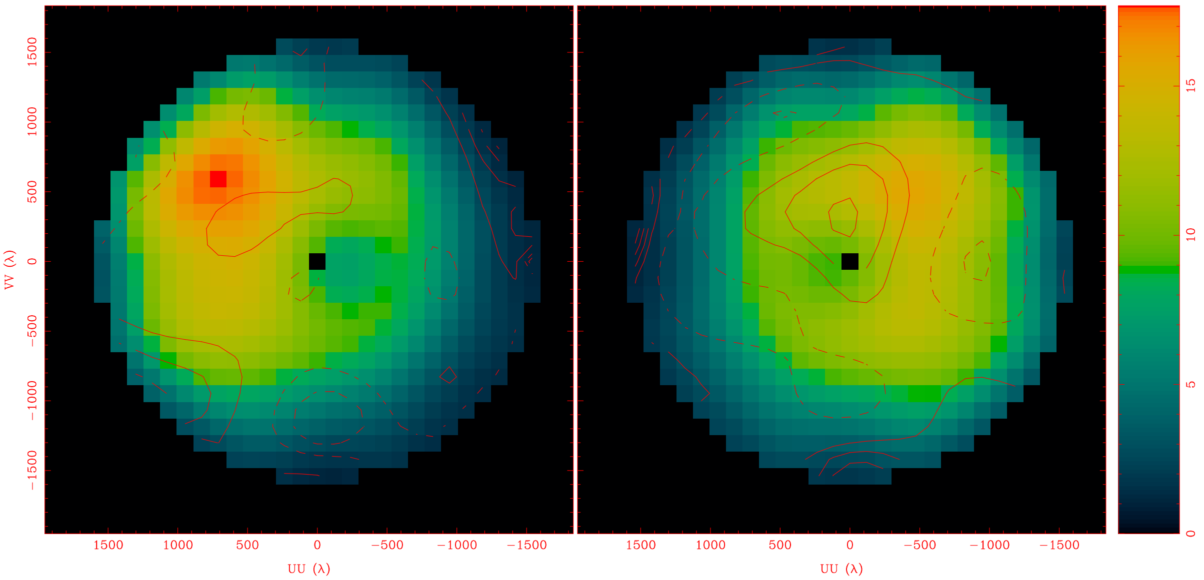

Figure 2.3 The left panel is pre-adjustment while the right panel is post-adjustment. Contours are in intervals of 25μm with dashed contours being negative and solid contours being positive. The color scale is the illumination pattern. The axes are in wavelength units were the wavelength is ~3 mm in these observations. There are few significantly deviant panels in the regions where the surface is well illuminated. However, alignment of the optics improved significantly after adjustment.

Figure 2.4 displays a representation similar to Figure 2.3 but for C1. Since C1 appeared to be reasonably aligned in the first measurement, no adjustment was made and any deviations represent the repeatability of the measurement. Initially, the offset was between 0.27 and 0.43 m at an angle between 2° clockwise from up and 20° counter-clockwise from up. More recent measurement suggests that this offset may have become more significant and that the angle may also deviate significantly. This indicates that there may be some long-term, time-variable component to the offset in alignment.

In general, the 6.1 m antennas display more well-centered patterns. Figure 2.5 (C10) and 2.6 (C9) show the most deviant and most well aligned 6m illumination patterns, respectively. Here the data are taken 2006 June 12 and 22 for C9 and 2006 May 10 and June 12 for C10. For C9, the offset is $\leq$0.1 m with a poorly determined

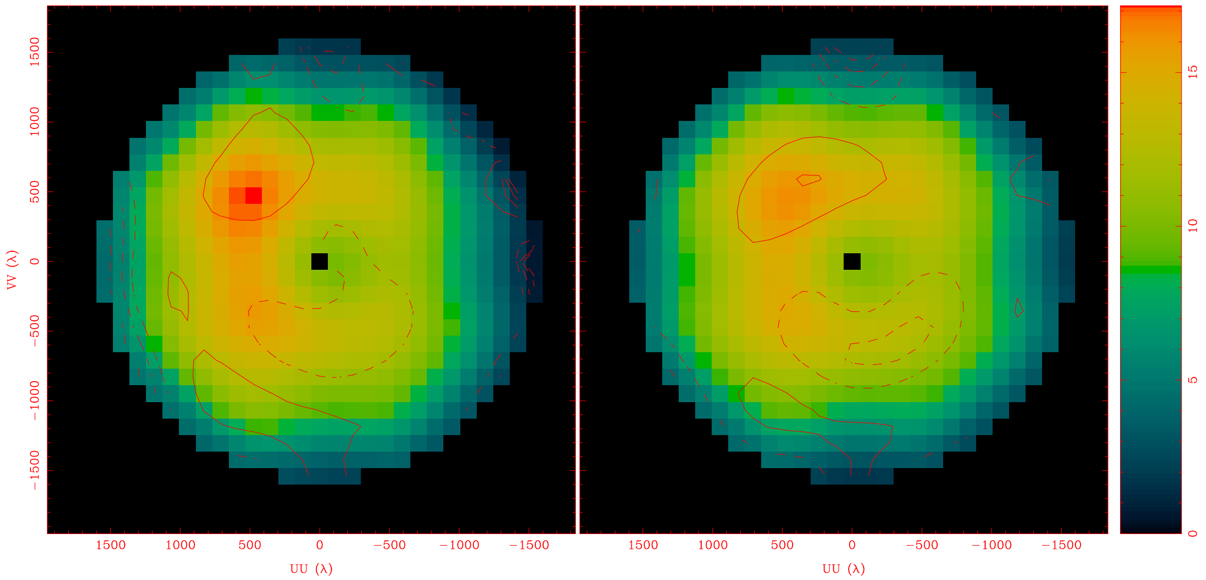

Figure 2.4 Similar to Figure 2.3 except for C1.

offset angle. For C10, the offset is between 0.11 and 0.13 m at an angle of 13 to 30° clockwise of up.

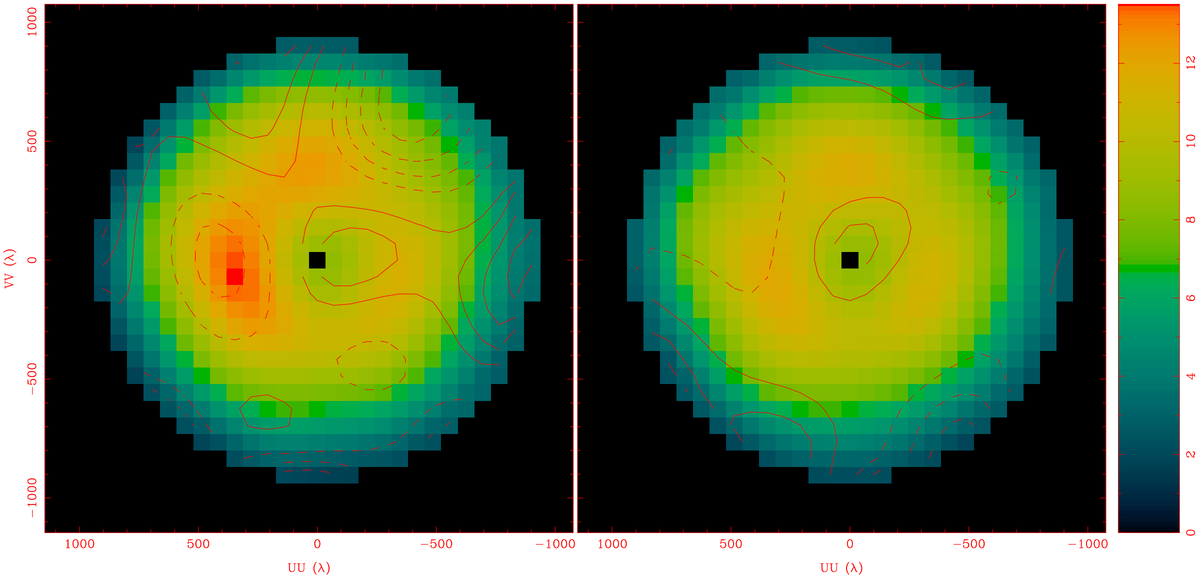

Figure 2.5 Similar to Figure 2.3 except for C10.

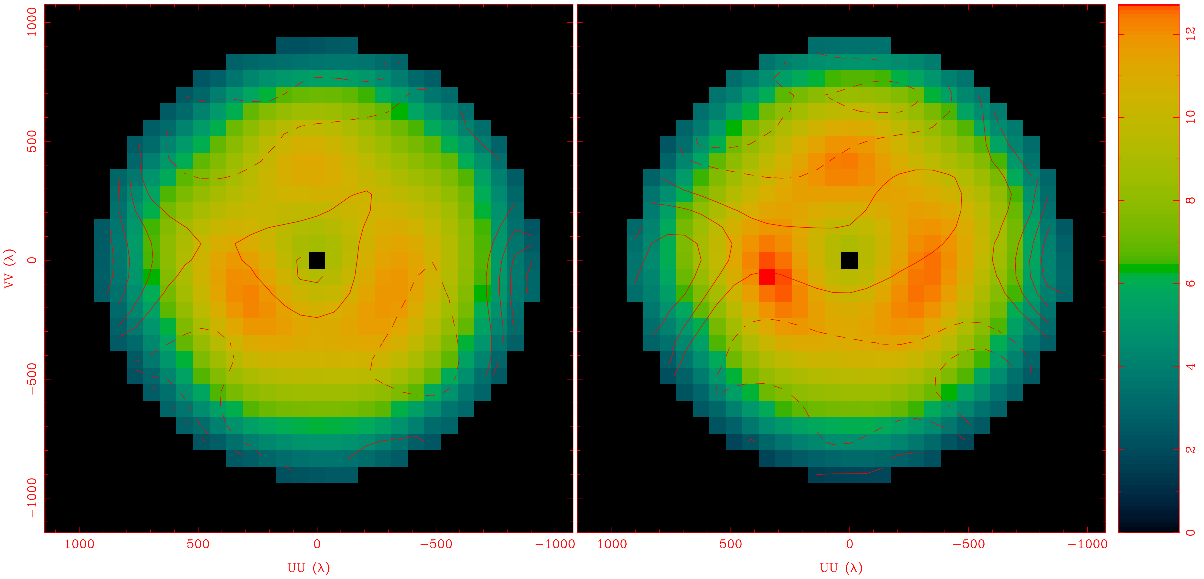

Figure 2.6 Similar to Figure 2.3 except for C9.

Table 2.2. Adjustment and Alignment Results

Antenna	Offset[a] meters @ °	Offset[b] meters @ °	Surface RMS[c] μm	Surface RMS[d] μm
1	0.43 @ 2	0.27 @ -20	28	27
2	0.28 @ -70	0.28 @ -41	40	40
3	0.29 @ -72	0.13 @ -49	31	31
4*	1.00 @ -24	0.46 @ 26	29	27
5	0.36 @ 20	0.36 @ 54	40	41
6*	0.69 @ -71	0.32 @ -40	33	29
7**	0.09 @ -26	0.13 @ -84	51	31
8**	0.14 @ -37	0.24 @ -37	50	29
9	0.02 @ 2	0.10 @ 82	31	39
10**	0.13 @ -77	0.11 @ -60	44	30
11**	0.09 @ -39	0.13 @ -16	43	29
12**	0.09 @ -53	0.10 @ 13	115	30
13**	0.17 @ -55	0.22 @ -60	54	23
14**	0.09 @ -75	0.12 @ -70	35	30
15**	0.13 @ 14	0.12 @ -83	33	25

Note. — Offsets are given by the calculated centroid and a correction factor for obstructed 2-dimensional Gaussian patterns (~13%). Angles are positive clockwise from up. Antennas denoted by * had alignment intentionally adjusted between trials. A change of receiver can also result in small changes to the centering of the illumination pattern. Antennas denoted by ** had panel adjustment performed. Columns 2 and 4 are for trials prior to any adjustement while columns 3 and 5 were post alignment/panel adjustment. Antenna 3 data has a very long time baseline (1.5 years) between measurements due to a variety of issues.

Table 2.2 presents the alignment measures for various antennas. Only two antennas (C4 and C6) were intentionally adjusted. Six antennas have imaginary voltage patterns that are consistent and measurable in the aperture plane. However, when comparing to the benchmark, only four antennas, C1, C4, C5 and C6, fail the criterion. The other two antennas, C10 and C11, will contributed fractionally small imaginary components which will only become significant in cases of extreme dynamic range.

2.3.2 Panel Adjustments

For the 10.4 m antennas, the panel adjusters are about a meter apart. and the modest-resolution holography is sufficient to determine both the need for panel adjustment and the adjustments themselves. The results in Table 2.2 indicate that there is little need for panel adjustment when compared to the benchmark, with the possible exception of C2 and 5. The possibility of improving surface accuracy for these antennas is shown in Figures 2.7 and 2.8. Note the similarities between the most deviant, high illumination regions on the two datasets. Given the nature of the 10.4 m adjustment points, which is such that the intersection of panels has a single adjustment point for all adjacent panels, adjustment of any location requires a global solution and global adjustment. No adjustment of these antennas was performed though the repeatable points could be corrected.

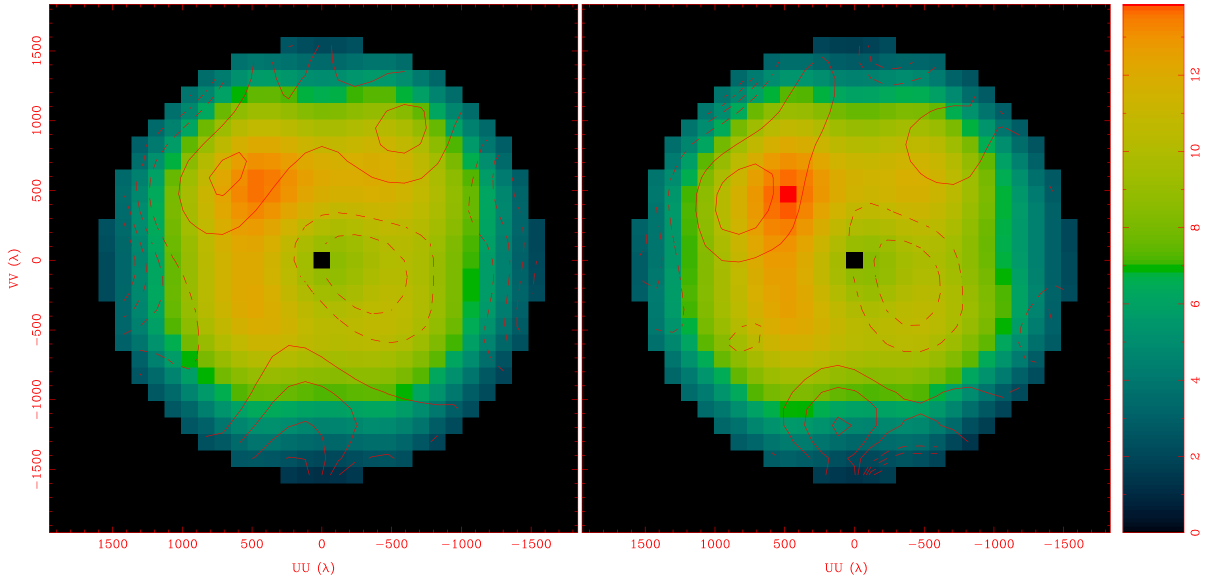

Figure 2.7 Similar to Figure 2.3 except for C2.

Table 2.2 shows a very different picture for the 6.1 m antennas. While the alignment is generally quite good, the surface RMS values typically did not meet the benchmark. The left sides of Figures 2.9 (C11) and 2.10 (C12) provide an illustration of the two typical modes of deviation for the 6m antenna surfaces. C11 shows localized deviations without significant large scale deviation. C12, on the other hand, shows a classic astigmatic pattern where the antenna is folded up along the axis left-to-right through the middle of the image which, in turn, depresses two other quadrants.

The adjuster locations on the 6.1 m antennas tend to be centimeters away from

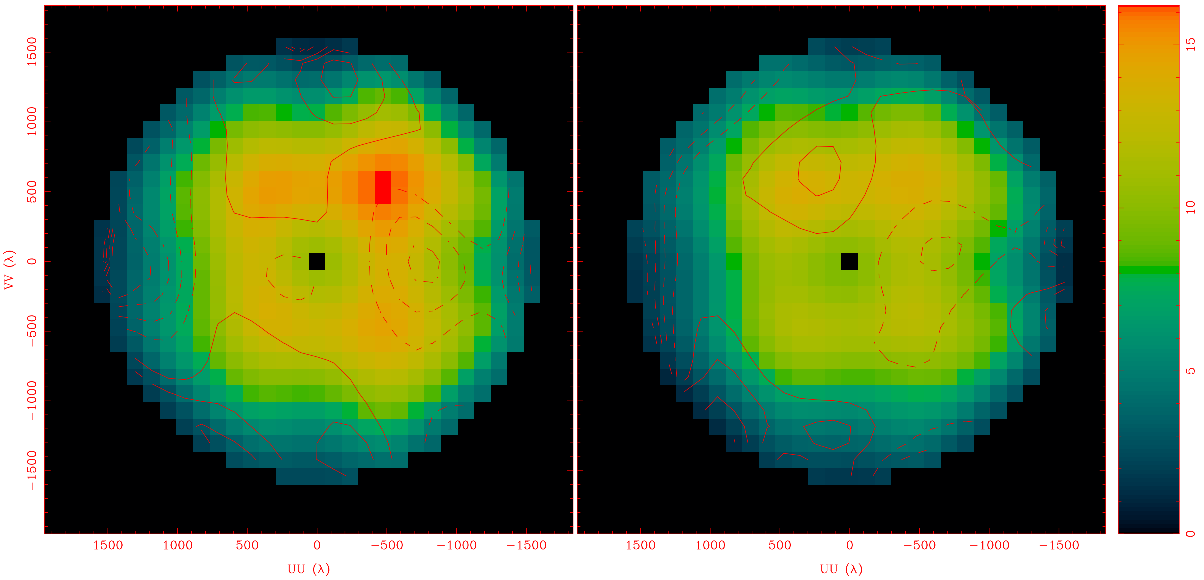

Figure 2.8 Similar to Figure 2.3 except for C5.

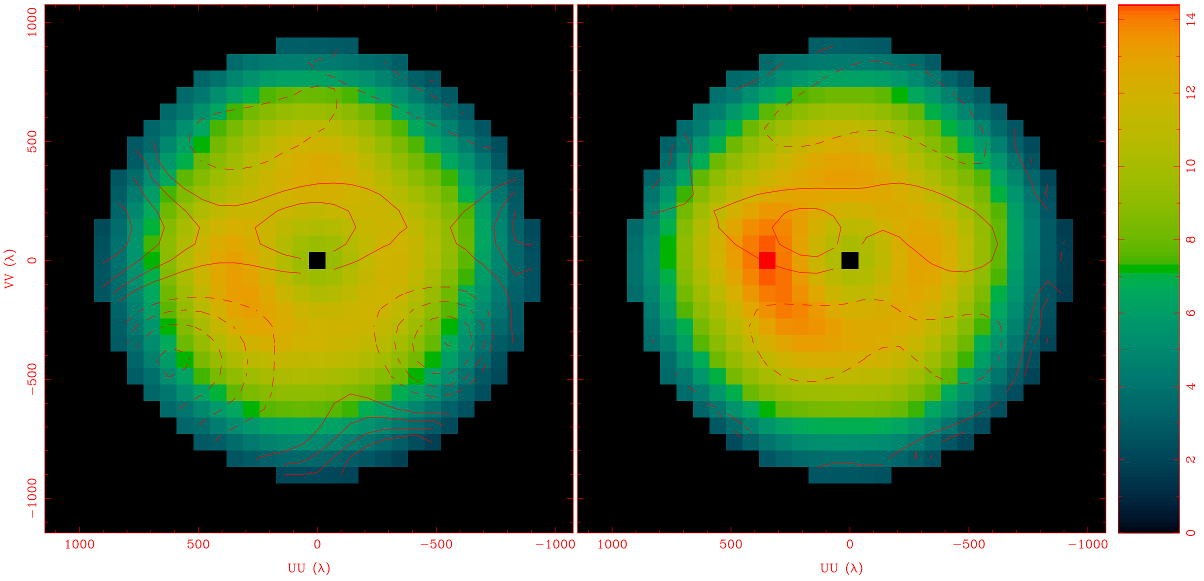

Figure 2.9 Similar to Figure 2.3 except for C11.

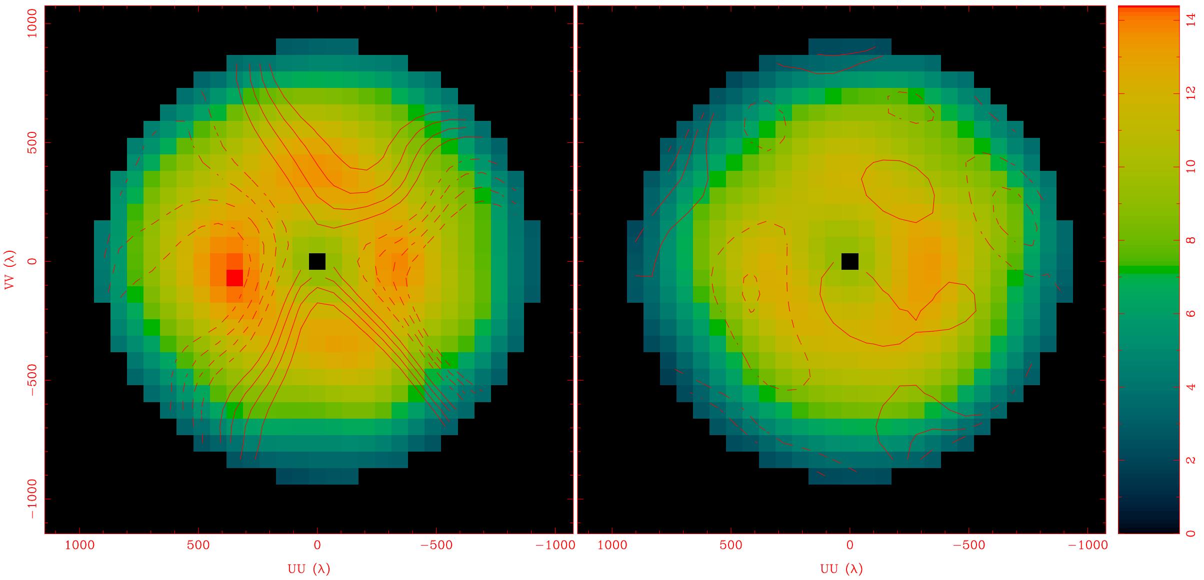

Figure 2.10 Similar to Figure 2.3 except for C12.

each other and each panel corner has its own adjuster. Figure 2.11 is an example of the maps used in carrying out the adjustments. To determine the adjustments needed, I interpolated the maps so as to achieve images well-resolved on the adjustment scale. Adjuster locations whose positions deviated by more than ∼60μm from the ideal surface on the amplitude and phase plots were corrected. Adjustments were carried out in steps of 5° using a dual-toothed tool that fits directly into the adjusters.

Given that the true resolution is far poorer than the inter-adjuster scale (centimeters), we adjusted the immediately adjacent adjusters by identical amounts. We expect that this technique should remove extremely large local deviation or large scale deformations. Resolution on the size scale of centimeters must await on-the-fly techniques and the use of the radio transmitter. Post-adjustment, these antennas show far less systematic deviation. The right-hand sides of figures 2.5, 2.9 and 2.10 show the typical improvement. Figure 2.6 was not adjusted and the data demonstrates the repeatability of our measurements. Table 2.2 presents the surface RMS after any adjustment.

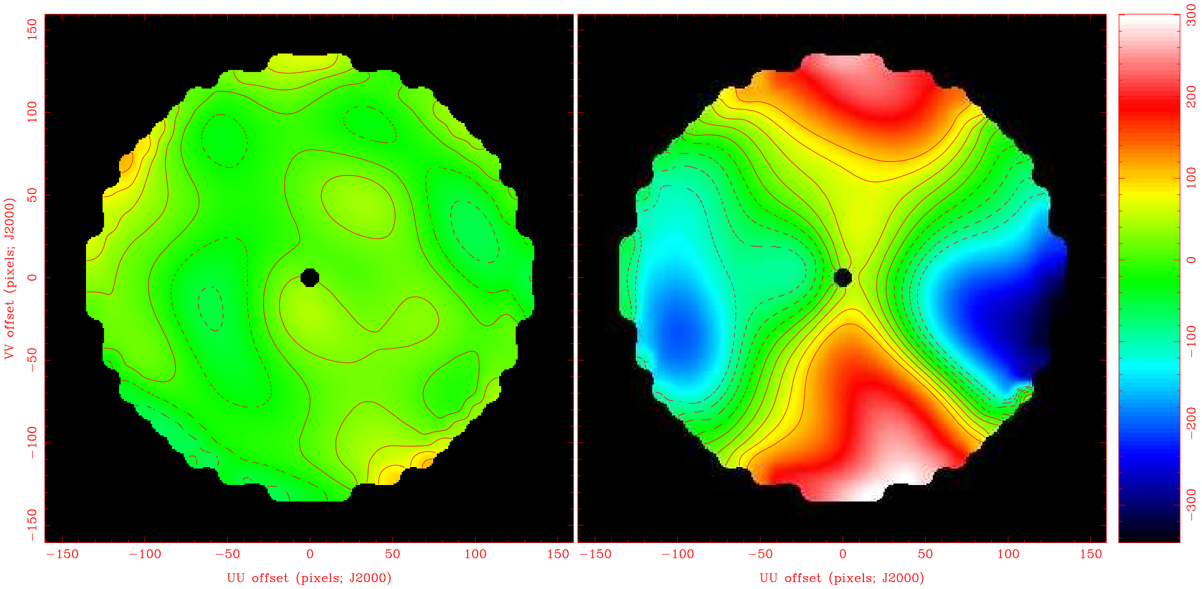

```
UU, VV, VELO = −6.92779167E−14     ixrelp, 6.92779167E−14, 7.32951E−14 km/s at pixel (321.00, 321.00, 1.00)
Spatial region : 161,161 to 480,480     Spectral inc/bin : 1/1 =1.804×10^-13/1.804×10^-13 (km/s)
Pixel map image: a12.regrid.cat (3C273)  Min/max=−345.9/300.9  Range = −345.9 to 300.9 microns (lin)
Contour image: a12.regrid.cat (3C273)  Min/max=−345.9/300.9 microns
Contours : −100, −75, −50, −25, 0, 25, 50, 75, 100
```

Figure 2.11 C12 is display prior to adjustment. Here, the contours are in degrees of adjustment needed given the 2.94μm per degree pitch of the adjuster screws.

2.3.3 Preliminary 1mm Results

Given the 1mm receiver positions in the dewar are not perfectly coincident with the 3mm receivers, the alignment can differ significantly between the 3mm and 1mm systems. The surface accuracy, however, is perfectly common to the two systems. Therefore, high- or modest-resolution holography is unnecessary at 1mm but low-resolution holographic data could help determine any independent deviation of the alignment of the 1mm system from the, aiding the aperture efficiency and image fidelity of 1mm observations.

However, valid, 1mm holography data are much more difficult to obtain. The required phase stability of the atmosphere for 3mm holography measurements is similar to that for 1mm science data making the phase criterion for 1mm holography extremely strict. Repeated datasets are thus very difficult and expensive, observationally, to obtain at 1mm. However, a single, high-quality dataset could be useful for constructing model 1mm beam patterns and determining any offsets in the illumination patterns. To date, such high-quality data is only available on the 10.4 m antennas (see Table 2.1).

On average, the 10.4 m alignment is poor and is currently the subject of intense effort at CARMA. Figure 2.12 displays the aperture plane illumination pattern while figure 2.13 displays the resulting voltage patterns. None of the aperture plane images appear to be well centered though C2 is close. Antennas like C4 actually show some illumination of the primary by the first side-lobe of the feedhorn. Indeed, when examining the voltage patterns on the sky, we see instances of large gradients on C4, showing a $\pm 40\%$ imaginary contribution over the central parts of the beam. The poor centering of the illumination pattern results in poor aperture efficiency. Considering the equation 2.3 and Figure 2.13, the resulting primary beams will have large imaginary components and, as described in 1, will have a detrimental impact on image fidelity.

Antennas showing patterns significantly different from a straight gradient (e.g. C1 and C2) are either showing signs of higher order variations across the beam or noise effects as these antennas are comparatively well aligned and are on longer baselines at the time of observation. These variations underscore the difficulty in obtaining quality voltage patterns at 1mm and may be the result of pointing error in the reference antenna(s) and any, currently unknown, voltage pattern phase gradient. A first attempt to center C3 was made on 2008 March 27 and, while the alignment is not perfect, the improvement is substantial. Adjustment of C4 and C6 have also been made but to date no verification dataset is available. Further optimization of the alignment will require observations in our most compact configuration, likely to occur in the summer of 2008.

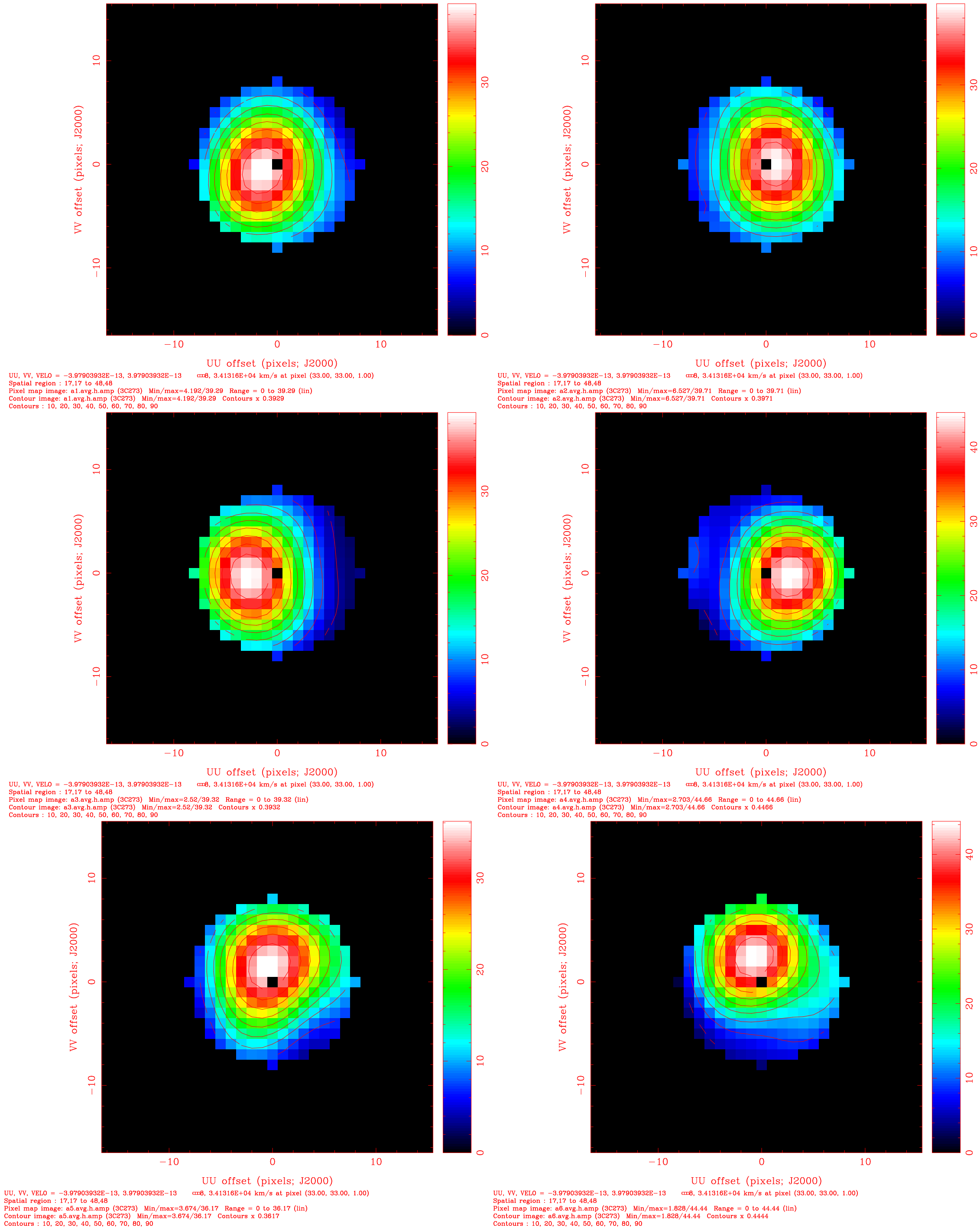

Figure 2.12 Each of the 10 m antennas is shown in the aperture plane. The color and contours both show the amplitude pattern with contours in steps of 10%. The offset from the center is large and obvious in most antenna patterns.

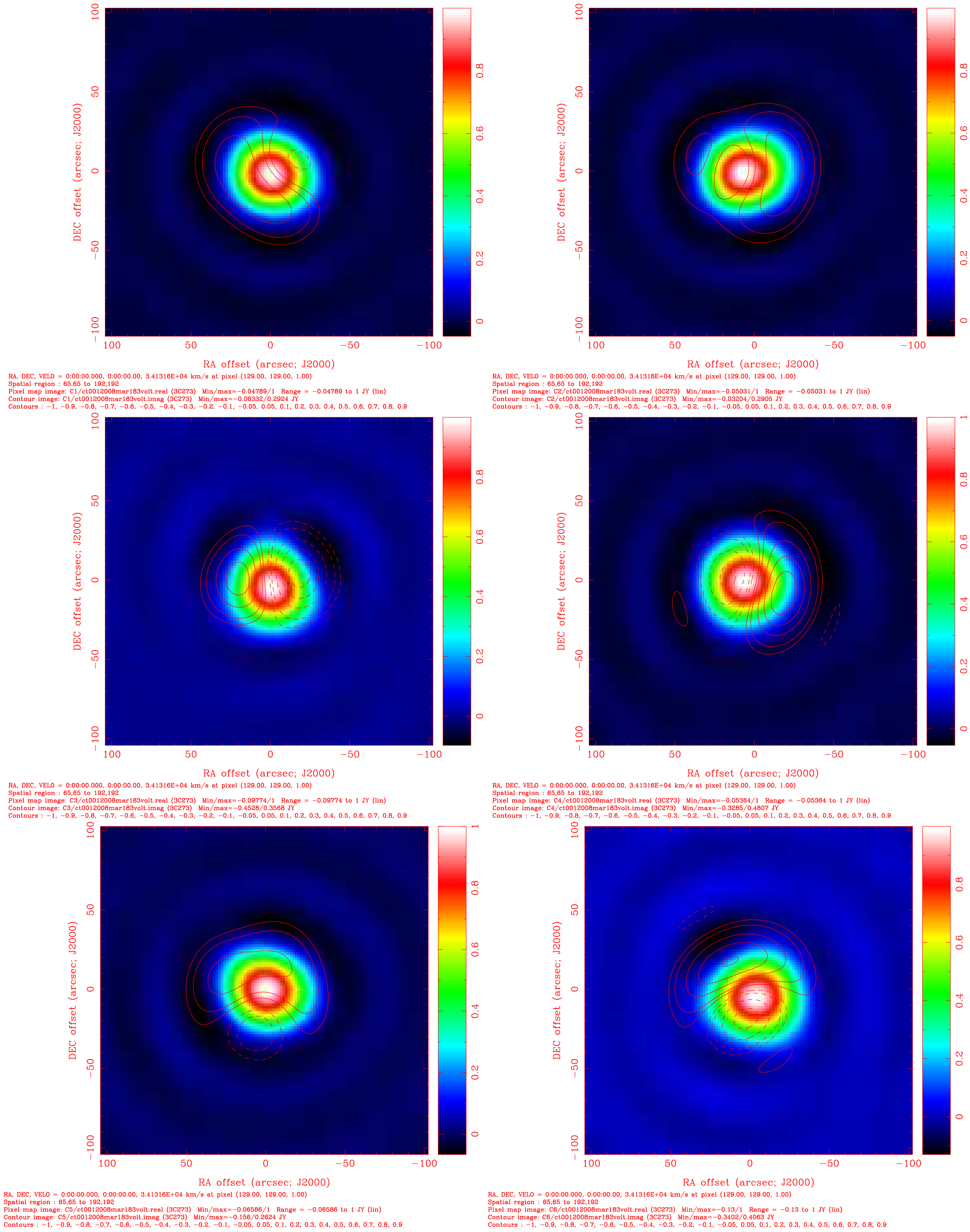

Figure 2.13 Each of the 10 m antennas is show in the sky plane with the real component of the voltage pattern show in color and the imaginary component shown in contours. The contours begin at 5% then 10% of the real component with intervals of 10% thereafter. The patterns are far more complicated given the large values of the offsets can result in more complicated patterns as feed sidelobes begin to illuminate the primary.

2.4 Holography Results: Shape and Consistency of the Voltage Patterns

After completion of the initial series of holography measurements to adjust panels and align optics, we began an additional campaign in an attempt to:

- **Address the accuracy of the assumed Gaussian profiles used in MIRIAD**
- **Address the applicability of the symmetric, Gaussian approximation to the primary beam profiles**
- **Determine any antenna or elevation based variation in the pattern**

Typical imaging software assumes the primary beam is uniform among antennas of a given style, is free of imaginary parts, and has a circularly-symmetric Gaussian profile. The first two goals address the properties of the antenna styles within the framework of typical assumptions. The results of such studies can immediately be integrated into the MIRIAD routine **pb.for** either by an alteration of the assumed width of the Gaussian model or by a replacement of the current, Gaussian model with a more relevant, but still uniform and circularly-symmetric, model. Pursuit of the third goal relaxes all of the typical imaging software assumptions. Particularly, relaxation of the *uniformity* condition can have dire consequences as imaginary components do not necessarily cancel upon creation of a baseline illuminating pattern, a primary beam in the traditional sense, for a given baseline, i.e. equation 2.3. When $m = n$ the imaginary components always cancel but for $m <> n$ the imaginary component can begin to strongly impact the image (see Chapter 1).

2.4.1 Data Acquisition and Reduction

Data collection and reduction was performed exactly as described as in §2.2 with the addition of few steps to recover the beam properties on the sky. The mean, masked real and imaginary aperture plane maps were padded with zeros using MIRIAD **imframe** and Fourier transformed, using **fft** in MIRIAD, back to the sky plane resulting in an interpolated voltage pattern on the sky with some noise filtering. To account for any frequency dependence between datasets, the cell sizes were scaled by the ratio of the frequency of the input dataset to the frequency of the fiducial frequency. The images were then interpolated to a common resolution on the sky using the MIRIAD task **regrid**.

Data described in Table 2.1 from 2007 and 2008 were utilized in the determination of mean voltage patterns though individual antennas were sometimes rejected for phase jumps or pointing drift problems. Pointing errors are highly variable from dataset to dataset, in collection of either science or holography data. In addition, such errors can be removed by a variety of means at the time of observation. I will discuss these methods in more detail later (see Chapter **??**) but for the determination of voltage patterns, pointing error was removed via recentering the patterns on the sky by using the MIRIAD routines **imgen** to create an approximate beam pattern on the sky but located at the image center and **imdiff** to determine the shift between the model and the true voltage pattern. The derived offset was applied to the true voltage pattern. Focus error, which is not easily determined at the time of observation, was not removed because these errors are present in the science data collection process and therefore the impact on the voltage pattern needs to be included.

2.4.2 Data Analysis

The MIRIAD task **imfit** was used to fit Gaussian profiles to the measured primary beams and provides major axis, minor axis, position angle and associated uncertainty. The axes were geometrically averaged to provide an estimate of the voltage pattern size. The ratio of major to minor axis defines the ellipticity. Fits to both the *real* and *amplitude* components were done because the *real* patterns tend to be more stable but the *amplitude* patterns contain a better representation of the instantaneous voltage response. *Amplitude* patterns include *imaginary* contributions, which tend to be more time variable due to changes in focus, astigmatic or coma induction from gravity in the antenna surface, or a time variable illumination pattern offset (i.e. time variable optical alignment due to motion of the secondary). The MIRIAD task **pbplot** was used to plot comparisons to the default models for the beams. Azimuthally averaged profiles were generated with the MIRIAD function **ellint** which integrates over annuli.

The real voltage patterns were fit with a variety of clippings. The clip value is surprisingly important to the determination of the width of the voltage pattern. Voltage patterns are multiplied by other voltage patterns to create the traditional *primary beam* for a given baseline. The fact that this is a baseline based parameter is of great consequence. Typically, the primary beams are clipped at the 5% point as the beams are thought to vary dramatically below this level. Inclusion of lower points on the beam (ref,ref) can improve image quality if those points are stable. For a homogeneous array, or in the case of CARMA for 10.4 cross 10.4 m baselines or 6.1 cross 6.1 m baselines, the primary beams are voltage patterns squared. This then requires that the voltage patterns be constant to the 22% level. However, for mixed baselines the 5% location in the primary beam is given by:

$$\vec{u}(PB_{mn} = 5\%) = 1.6 * \frac{(F_1^2 + F_2^2)^{0.5}}{F_1 F_2} \tag{2.7}$$

for antennas having voltage patterns of FWHM F_1 and F_2. At this point, the 6.1 m antenna voltage patterns only need to be consistent to ∼50% but the 10.4 m antenna must be consistent at the ∼10% level. Inclusion of even smaller antennas, e.g. the 3.5 m SZA antennas which will soon be relocated to Cedar Flat, requires consistency of ∼10% and ∼5% for the 6.1 m and 10.4 m voltage patterns, respectively. Therefore, I fit the voltage patterns with clippings of 22%, 10% and 5%.

Fits to the imaginary beams were done by identifying maximum and minimum of the imaginary pattern. The half peak-to-peak was then calculated. The position angle of the line connecting the positive peak to the negative peak was also determined. Finally, the location of the imaginary peaks within the real pattern is calculated as an average of real beam at the imaginary maximum and minimum. The first two parameters identify the magnitude of the imaginary component and its location while the last value estimates the importance of the imaginary component to the overall

Table 2.3. Mean Parameters of Antenna Styles

Style	Clip %	#	FWHM Real ″	FWHM Amp ″	e Real %	e Amp %	PA Real °	PA Amp °
10.4 m	22	49	91.45 ± 1.20	93.22 ± 1.94	1.45 ± 1.12	2.78 ± 2.48	14.2 ± 50.9	17.9 ± 50.2
10.4 m	10	48	89.88 ± 1.12	92.46 ± 2.51	1.77 ± 1.26	3.19 ± 2.60	14.0 ± 57.1	18.2 ± 48.4
10.4 m	5	49	89.04 ± 1.08	92.22 ± 2.92	1.71 ± 1.51	2.93 ± 2.58	-11.9 ± 57.1	14.0 ± 47.5
10.4 m[a]	22	18	91.32 ± 1.03	92.05 ± 1.40	0.98 ± 0.67	1.76 ± 1.49	18.1 ± 59.1	22.8 ± 56.6
10.4 m[a]	10	18	87.71 ± 0.86	89.65 ± 2.27	2.42 ± 1.37	3.33 ± 2.10	-48.6 ± 53.8	17.3 ± 56.3
10.4 m[a]	5	18	88.88 ± 0.89	90.86 ± 2.34	1.43 ± 1.18	2.28 ± 2.33	-57.8 ± 41.7	31.9 ± 56.5
6.1 m	22	57	152.87 ± 1.94	154.68 ± 2.06	3.16 ± 2.47	3.17 ± 2.33	-5.8 ± 26.7	-8.4 ± 24.2
6.1 m	10	57	150.23 ± 1.84	151.94 ± 2.34	3.47 ± 2.39	3.29 ± 2.50	-10.2 ± 34.9	-12.5 ± 24.2

Note. — [a] indicates the exclusion of antennas known to have large gradients in the imaginary beam. # is the number of measurements included in the value given. Uncertainties are in the same, i.e. the standard deviation of the mean is the uncertainty quoted divided by the square root of #-1. Nominal amplitude beam size is 91.64” and 162.92” for the 10 m and 6 m antennas, respectively. Othqer imaging assumptions are such that the real component beam size and amplitude beam size are identical, and ellipticity is identically one. The position angle of the beam is expected to be near zero because the dish should deform top to bottom based on gravitational stresses resulting in an elongated beam in the elevation direction.

beam profile.

2.4.3 Gaussian Fits to Measured Voltage Patterns

To determine the Gaussian widths for comparison with the default voltage patterns, I apply the clipping at the 10 and 22% levels. Table 2.3 provides the measured values for the voltage pattern sizes for all relevant clippings and parameters for the 10.4 and 6.1 m *style* antennas, i.e. C1-6 and C7-15 considered as ensembles. Properties of individual antennas will be addressed later. For the purposes of CARMA, only the fits for the 6.1 m antennas at 22% and the 10.4 m antennas at 22% and 10% are significant. Fits at lower levels are relevant only with inclusion of the 3.5 m SZA antennas and that will be addressed separately.

2.4.3.1 10.4 m Antennas

Figure 2.14 shows the real (left) and amplitude (right) widths of the 10.4 m antenna voltage patterns clipped at 22%. These values for the width are most relevant for the primary beams created for the 10.4 cross 10.4 m baselines. The horizontal line shows the value provided by MIRIAD for the voltage pattern width. The amplitude pattern is wider on average for the 10.4 m. As will be shown below, this is due to large imaginary contribution from several of the antennas. Indeed, when only C2 and C3 are considered, the antennas without imaginary contributions, the amplitude patterns are only marginally larger and nearly identical within the spread.

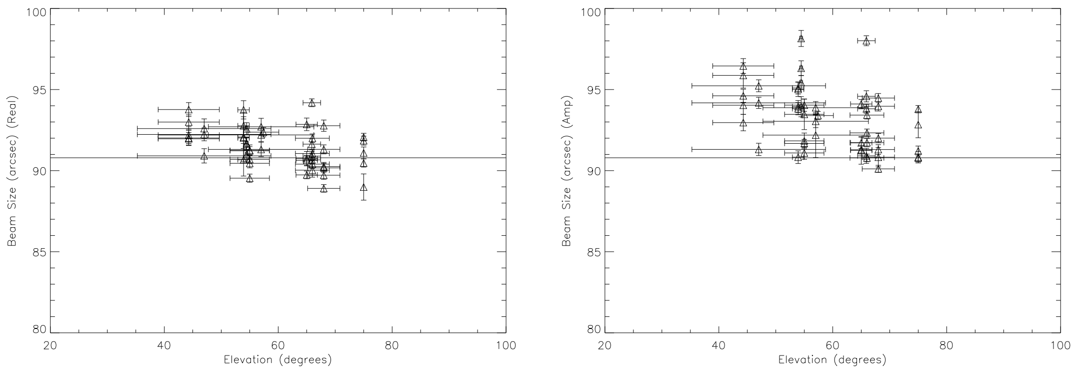

Figure 2.14 The real (left) and amplitude (right) voltage pattern sizes are plotted as a function of elevation. Data from C1-6 are included here. The horizontal axis is the elevation with error bars representing the range of elevation over which the data was collected. The vertical axis is the voltage pattern size with error bars propagated from the **imfit** fits to the axes. The solid line represents the default width from MIRIAD and is 91.64".

The real voltage pattern width, clipped at 22%, has standard deviation of the mean within 1σ of the default model from MIRIAD. The width of the amplitude pattern of the ensemble is ~1.5% wider than the default pattern and more significant in the mean, with a 5.5σ difference. However, if I consider only antennas C2 and 3, the antennas without significant imaginary contribution, the deviations with the default model because vanishingly small. These deviations are insignificant when considering detriments to image fidelity (see Figure **??**), indicating that the default FWHM for the Gaussian model in MIRIAD is accurate for the 10.4 cross 10.4 m baselines.

Figure **??** shows the voltage pattern fits clipped at the 10% level for the real (left) and amplitude (right) components. There is some hint of a narrower voltage width in both the amplitude components. This change is also evident in the fits excluding antennas with imaginary components. The deviations of the amplitude component is not statistically significant, but the real component is smaller than the MIRIAD model at the 11σ level in the mean. The difference (2%) is still small compared to the standard deviation of the sample and is small in terms of the possible detriment to image fidelity (again, see Figure **??**).

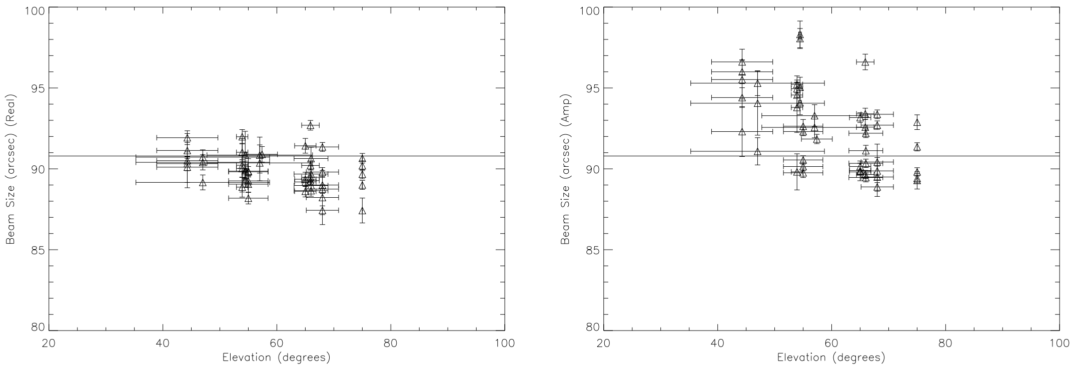

Figure 2.15 Similar to 2.14 except clipped at the 10% level. The default size, shown as the horizontal line, is 91.64".

In both components, there is some evidence of changes in width as a function of elevation. As the antenna moves to lower elevation, the top and bottom portions of the dish are subject to additional strain and may begin to sag. One could envision a situation where the voltage pattern becomes larger in the vertical direction and the ellipticity becomes larger with a relatively constant position angle. However, the bulk of this trends sits within the scatter of the measurements and a linear fit to the data reveals that a constant fits within one sigma.

In terms of the width of Gaussian fits to the voltage pattern, the default values in MIRIAD are acceptable for inclusion in both the 10.4 cross 10.4 m baselines and the 10.4 cross 6.1 m baselines. However, the narrowing of the pattern at increasingly lower levels indicates that the voltage pattern may get narrower more rapidly than the Gaussian model.

2.4.3.2 6.1 m Antennas

Figure **??** shows the real (left) and amplitude (right) widths of the 6.1 m antenna voltage patterns clipped at 22%. The 10% clipping is discussed later in the context of the SZA antennas. These values for the width are most relevant to the baselines created for 6.1 cross 6.1 m baselines and 10.4 cross 6.1 m baselines. The solid line shows the value provided by MIRIAD for the voltage pattern width.

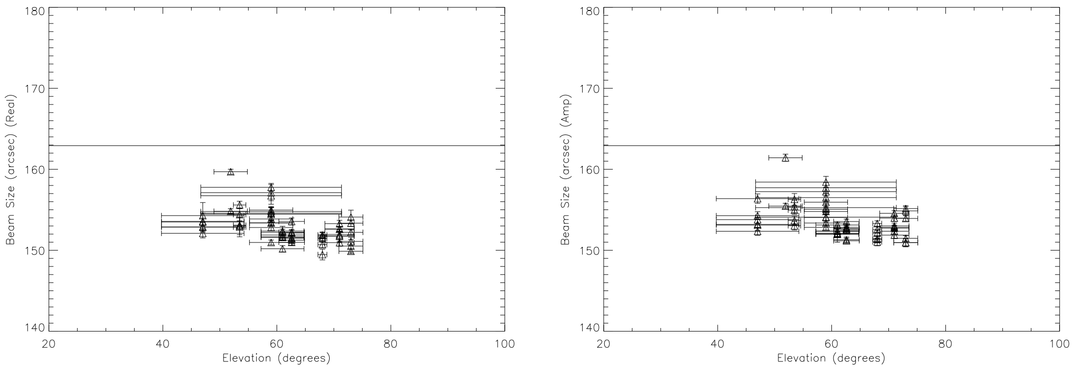

Figure 2.16 Similar to 2.14 except for the 6.1 m antennas. The default size is 162.92".

The amplitude and real patterns are consistent within the standard deviation of the samples. Here the deviation from the default MIRIAD model (162.9") is significant. The measured width of the amplitude component is 154.7±0.2" for the uncertainty in the mean. This 5% difference has significant impact on the image quality (Figure **??**). The default FWHM in MIRIAD has been altered to account for these differences. Like the 10.4 m antennas, the 6.1 m antennas show evidence of a narrowing voltage pattern relative to a Gaussian at low levels. These antennas also show a possible trend with elevation, but, again, the significance of the trend is weak.

2.4.3.3 10.4 m Cross 6.1 m Baselines

The heterogeneous baseline creates a voltage pattern that looks like the square root of the product of the 10.4 m and 6.1 m voltage pattern on the sky. The product of two Gaussians produces another Gaussian, with $\frac{1}{FWHM_{new}^2} = \frac{1}{FWHM_1^2} + \frac{1}{FWHM_2^2}$ and the resulting voltage pattern width is then $\sqrt{2}FWHM_{new}^2$. Given equation 2.7, the fit to the 10.4 m voltage pattern must be considered down to the 10% level. The value given by MIRIAD for the default model is 117.10". For the values derived above, the resulting width should be 111.50". The 5% devivation from the default model will have a significant impact on the image fidelity (see Figure **??**). The values within MIRIAD have been changed to account for this difference.

2.4.4 Deviation from Circularly-symmetric, Gaussian Fits

2.4.4.1 Deviation from Gaussians

Figure 2.17 shows the amplitude of the mean primary beams (top) for the 10.4 (left), heterogeneous baseline (center) and 6.1 m (right) antennas, respectively. These were formed by averaging antennas of a given style over time and antenna number. The second row depicts the azimuthally averaged version of the images shown on the top row. The dashed-line represents best-fit Gaussian to the average image. The dotted line shows the MIRIAD model. The horizontal lines show the half-power, 5% and 1% points in the primary beam. The next two rows highlight specific regions of the beams and the last row, now in linear scale, show the differences between the MIRIAD model and the data (dotted line) and the best-fit Gaussian and the data (dashed line).

At the half power point, the 10.4 m beam is well fit by the MIRIAD model. The measured profile is actually wider at the half power point than either of the best-fit Gaussian models. This difference is offset at lower levels in the beam. As discussed above, the width of the best fit Gaussian is far-narrower than the MIRIAD model for the 6.1 m primary beam. The apparent difference seems to be mitigated to some extent here but but the difference above was discussed in terms of FWHM of the voltage patterns and the difference here is radial differences in the primary beam so differences are suppressed by a factor of $2\sqrt{2}$. The width difference is similar in the mean profile compared to the fits to the ensemble discussed above. The same is true for the heterogeneous baseline.

The previously identified apparent trend of the voltage patterns getting narrower faster than a Gaussian at low levels is clear in the azimuthally averaged profiles. In the case of beam primary beam, the 5% point (dot-dot-dashed, horizontal line) shows that the Gaussian lies far outside the value for the data. In the best case scenario, the 10.4 m antenna primary beam is actually slightly wider than the predicted Gaussian at the half-power point and then narrows rapidly. At the 5% level the measured profile is 3-3.5" narrower. This difference grows to 5-9" for the 6.1 m primary beam depending on whether the MIRIAD model or the best-fit Gaussian is used. The difference at the 5% level for the heterogeneous baseline is between 6 and 10.5". Deviations at the 1% level will be discussed with the along with the sidelobes later.

In reality, the Gaussian model represents a compromise averaged over the entire beam. The Gaussian initially gets narrower faster than the measured profile but then the measured profile decreases rapidly causing the Gaussian to under-predict the power at the half power point of the beam but eventually it over-predicts the power in the wings of the profile. The best-fit averages these contributions with the half-power point providing more power but the wings covering a much larger area. This trend is seen in the residuals as a function of radius shown in Figure 2.17.

I can estimate the deviation from the model by integrating the absolute value of the residual profile or by weighting by either the amplitude or the amplitude times the are of a given annular region. For the 10.4 m antenna, the best-fit Gaussian (dotted line) produces less error in the core of the beam but more in the wings. All weightings show that the best-fit Gaussian produces less error than the MIRIAD model but the difference between the models themselves is never more than ~1%. For the 6.1 m antenna, the improvement is far greater except in the very central portions of the beam. Here, the use of a wider beam profile by MIRIAD better approximates the very central regions of the beam but near the half-power points, the deviation is more significant. Weighting the profile by the symmetrized beam shows only marginal improvement of the best-fit Gaussian over the MIRIAD model but weighting by the beam and area shows dramatic improvement. A similar situation is seen for the heterogeneous baseline. Clearly a different model of the primary beam is needed if the discrepancies are to be rectified.

IF TIME ALLOWS I WOULD LIKE TO FIT THIS TO SOME FUNCTION LIKE THE VLA DID BUT I HAVE MADE THIS SO I DON'T HAVE TOO. I WILL REFERENCE AN APPENDIX HERE IF I GET IT DONE...IF NOT I LEAVE IT OUT.

2.4.4.2 Ellipticity

Departures from circular symmetry in the core of the beam are expected. The dish is expected to sag somewhat under the influence of gravity elongating the beam in the vertical direction as the top of the dish sags slightly towards the ground. Differences in the ellipticity of the real and amplitude component are expected when the imaginary component of the beam dominates as this extends the amplitude beam in the direction of the imaginary component. The ellipticity is also expected to change as a function of elevation with ellipticity growing at lower elevations because of increased sag. Exclusively amplitude ellipticity, excited by an imaginary component, will be discussed in the context of the imaginary beam later.

As an ensemble, there is little evidence of ellipticity in the 10.4 m antennas. Figure **??** shows the ellipticity (top) and position angle (bottom) for the 10.4 m antennas. The left column is the real component while the right side shows the amplitude component. The average ellipticity derived for the amplitude component, 1.12±0.4%, is 3σ consistent with zero. The real component ellipticity, 1.94±0.2, appears to be significant but the spread in the sample of position angles, ±51°, leaves little doubt that the ellipticity is not real as the position angle is symmetric about ±90°. It is possible that there is some significant ellipticity but it is masked by imaginary beams which, for the purpose of this work, are antenna based parameters.

Figure **??** shows similar data to **??** but for the 6.1 m antenna voltage patterns. Here, the ellipticity is consistent in the real and amplitude components, with values

3.2±2.5 -6±27° and 3.2±2.3 -8±24°, respectively. The consistency of the real and amplitude ellipticity, and the consistency and relatively small spread of the position angle suggests that this ellipticity may be inherent to the 6.1 m antennas. If we calculate the standard deviation of the mean for these values brings the values to 3.16±0.33 -5.8±3.6° and 3.17±0.31 -8.4±3.2° for the real and amplitude patterns. The values are consistent with a 3.2±0.3% ellipticity at an angle 3σ consistent with zero position angle. There is no evidence of ellipticity changing with elevation but the precision of the measurements here may mask such a trend.

The position angle of the ellipticity will rotate on the sky with parallactic angle and therefore requires a more detailed treatment of the imaging process than software currently allows. In chapter 1 I developed the tools for addressing the ellipticity via simulation and in chapters **??** and 3 I apply this to actual data.

2.4.4.3 Low Levels and Sidelobes

The inclusion of the 8-element, Sunyaev-Zeldovich Array (SZA) into CARMA (hereafter CARMA-23) provides an excellent opportunity to enhance wide-field imaging capabilities. A single 10.4 m cross 3.5 m antenna baseline is nearly equivalent to a 6.1 m cross 6.1 m baseline and 48 such baselines would represent a non-negligible enhancement to the overall sensitivity, especially to large scale structures. The inclusion of the SZA more than doubles the instantaneous uv-coverage, from the 105 baselines of the current array to 253, and the 3.5 cross 3.5 m baselines can probe flux on scales of 2-3'. Enhancing the uv-coverage on these very large scales will enable recovery of the remaining, largest spatial scales, by the 10.4 m antennas in total power. All told, the wide-field imaging power of CARMA will be greatly enhanced.

However, there is a concern. The voltage response of the 3.5 m SZA antennas is wide, with a 4' FWHM at 3mm. The 10.4 m antennas, with FWHM of ∼1.4' at the same wavelength, have sidelobes well within the 3.5 m antenna main beam. Ordinarily, in homogeneous arrays, the primary beam for a baseline has the sidelobes of one antenna illuminated by the sidelobes of the other so the sidelobes are highly suppressed relative to the main beam. In the case at CARMA, even the first sidelobes of the 10.4 m antenna voltage pattern are illuminated by the main lobe of the 6.1 m antenna voltage pattern at the 20-25% level. Figure 2.20 demonstrates both the small influence of the 10.4 m antenna voltage pattern sidelobes when illuminated by a 6.1 m antenna voltage pattern (left panel) and the larger influence when that illuminating voltage pattern is changed to one generated by a 3.5 m antenna (right panel). The residual contribution from the sidelobes increases by a factor of three from an often negligible ∼3% to a hard to ignore ∼10%.

If the 10.4 m antenna voltage pattern sidelobes are neither stable nor predictable, the benefit of the SZA will be restricted as 10.4 m cross 3.5 m baselines will not be included resulting in a loss of 30% of the improved instantaneous uv-coverage and substantial reduction in improved sensitivity. Modeling the behavior of the sidelobes and determining their overall stability at a level necessary for high fidelity imaging is an expensive enterprise, requiring repeated, modest-resolution holography over a variety of observing conditions spanning day-time and night-time conditions. However, an initial estimate of the stability can be made with our current, night-time restricted dataset. While I would hesitate to use the beams described here for imaging, I can verify whether more detailed study of the sidelobes is merited.

Figures **??** and **??** displays the intra-antenna variation of the six 10.4 m antennas in the real and imaginary component, respectively. The averaged (real-only) sidelobe pattern is visible in 2.17 though the relevant quantity now is the square-root of the displayed primary beam. The dataset from 2008-Mar-24 (see Table 2.1) was used as the base image as this was the dataset which included the greatest number of 10.4 m antennas. Data from 2007-Aug-12, 2007-Sep-07, and 2008-Mar-27 at 3 mm was used for comparison. C1 uses data from 2007-Sep-07 as the template and only 2007-Aug-12 is available for comparison, and, in the following discussion, it is largely ignored due to the lack of sufficient data for comparison.

In general the agreement between the various real components is remarkable. The bulk of the sidelobe pattern subtracts out extremely well, with voltage pattern sidelobes of 5-10% being typically consistent to within <2-3% of the voltage pattern peak. Given the nominal beam patterns are assumed to be Gaussian and have no sidelobes, use of an appropriate model of the sidelobes can easily reduce the error induced by using this Gaussian from 5-10% to 2-3%, an improvement of a factor of 2 to 5 even without a detailed treatment of the sidelobe variations with time or observing conditions.

Instances of 5% or more deviation are rare, with C2, C3 and C4 showing single instances of such deviation. For all but C4, these differences are common to the datasets separated significantly in time indicating that there may be time evolution involved or that the more significant deviations seen in the red and cyan contours may be related to the marginally resolved source used in these beam patterns. The RMS of the residual images is always less than 0.9% with datasets taken more closely in time reducing this deviation to 0.8% or less. The largest deviations are seen near the half-power point of the illuminating, 3.5 m antenna voltage pattern indicating that, while the overall consistency of the real component of the voltage pattern is strong, work remains to be done.

The agreement of the various imaginary components is less striking. In general the signal in the imaginary beam is rather small. In Figure 2.22, the peak signal is typically 0.2, i.e. ±20% of the nominal beam peak. Variations in the imaginary beam in C1 are 3-5% out of 20%, i.e. still showing the signal is significant. The receiver in C2 was changed between the taking of the data shown in red and cyan contours and the data shown in the template and green contour data. The old receiver had significantly higher noise than the other antennas and the more recent data is more likely to represent the true repeatability of the voltage pattern. C2 and C5 have structures which appear to be constant phase offsets and are likely the result of poor phase stability during the observation.

The structure of the 10.4 m antenna main lobe voltage pattern also needs to be consistent down to the 5% point in the pattern. Table 2.3 and Figure 2.17 display the properties of the main lobe down to this level and beyond. Clearly, CARMA-23 will require the new model for the primary beam profile to be implemented. The 5% point in the voltage pattern is the 0.25% point in the voltage pattern, i.e. at the vertical position where the first sidelobe peaks. At this point, the main lobe deviates from the Gaussian model by 20" or more. The fact that, as ensembles, the Gaussian fits to the width get smaller at lower levels implies that all of the antennas will show a faster decrease in the voltage pattern than a Gaussian would predict.

It appears as though further effort to measure and monitor the sidelobes and the low power levels of the voltage pattern is merited based on the consistency seen in these datasets and the measured profile. Such a monitoring campaign serves two purposes. First, it provides an opportunity to monitor the properties of the beams and may catch sudden changes in focus and determine if sudden changes in aperture efficiency may be likely while simultaneously providing the means by which to correct such issues. Second, it allows a build-up of beam profiles which would provide a long time baseline spanning a variety of observing conditions which will be vital to obtaining high image fidelity in the future.

2.4.5 Antenna Based Results

I now break down the voltage pattern fits described above into antenna based phenomena. The results for individual antenna voltage patterns are provided in Table 2.4. The table provides information on the number of relevant datasets per antenna along with derived properties. As was the case for the ensemble properties, the uncertainties quoted are of the sample, not the mean, unless otherwise stated. Three additional parameter are added here, namely the magnitude of the imaginary beam as calculated by half the difference between the maximum and minimum contribution, the position angle of the line connecting the maximum and minimum, and the magnitude of the mean value of the real beam at the location of the imaginary maximum and minimum.

While the number of datasets available for a given antenna style is typically rather large (∼50), several antennas were offline for large portions of the summer of 2007. Antennas 8 and 15 were subject to massive errors in the pointing model resulting in pointing *drift* during the observations. Such pointing drift does not simply result in the offset of the beam center but shears the beam and can result in alteration of any

Table 2.4. Voltage Pattern Parameters

Ant#	#	FWHM Real ″	FWHM Amp ″	e Real %	e Amp %	PA Real °	PA Amp °	Peak to Peak Imag	PA Imag °	Real @ Rea
1	7	88.91±1.10	91.16±2.24	2.1±1.3	2.8±1.1	14.8±33.7	1.4±16.8	0.163±0.023	151.0±11.0	0.542±0
2[a]	7	90.42±0.63	91.98±2.04	1.8±1.1	3.5±2.2	-39.0±50.8	-67.1±23.4	0.091±0.040	123.5±86.2	0.398±0
3	11	89.33±0.91	90.56±1.59	1.1±0.6	1.7±0.7	53.4±49.1	-2.3±2.2	0.086±0.045	-96.9±81.8	0.379±0
4	8	91.45±0.71	95.03±1.98	2.0±1.2	3.7±3.4	35.1±42.0	-65.6±5.8	0.172±0.042	-58.1±11.0	0.542±0
5	9	89.74±0.64	92.55±2.13	1.5±0.7	3.3±2.9	-17.3±34.3	59.5±8.0	0.169±0.052	-125.8±47.7	0.510±0
6	6	89.50±0.54	94.48±2.08	2.8±2.3	5.4±3.7	55.2±21.6	40.9±13.5	0.221±0.028	-146.7±19.4	0.561±0
7[b]	3	153.18±1.27	153.15±0.88	1.2±0.7	2.8±1.8	-23.6±26.8	-23.5±29.1	0.055±0.013	-17.9±90.0	0.119±0
8[c]	5	152.62±2.53	152.74±2.58	3.3±1.5	4.5±3.7	-1.8±12.2	-0.5±12.8	0.057±0.013	83.9±76.3	0.475±0
9	8	152.44±1.32	153.23±1.49	3.7±4.3	2.9±2.4	-14.9±26.3	-12.7±9.8	0.062±0.007	81.3±57.4	0.342±0
10	9	153.06±1.76	154.24±1.91	3.1±2.0	2.3±1.5	-13.4±26.4	4.0±24.5	0.098±0.017	36.5±15.8	0.461±0
11	6	150.79±0.92	152.78±1.27	3.1±1.3	2.5±2.5	3.7±25.9	4.0±30.9	0.088±0.012	110.2±18.9	0.273±0
12	8	152.55±1.57	153.57±2.09	4.5±3.2	4.0±2.4	-13.8±26.4	-9.3±29.1	0.080±0.018	88.7±80.4	0.286±0
13	8	153.81±1.98	154.16±2.19	2.2±1.7	2.7±2.2	7.9±25.8	11.0±35.2	0.071±0.020	-2.5±49.9	0.394±0
14	6	152.65±1.06	153.26±1.17	3.4±1.6	3.4±2.9	-10.7±17.2	-20.8±25.1	0.067±0.010	42.9±79.9	0.356±0
15[c]	4	155.60±2.89	156.04±3.89	2.7±2.6	4.1±1.7	-17.6±16.9	-26.8±19.6	0.069±0.027	-82.7±100.3	0.266±0

Note. — MIRIAD amplitude beam size is 90.78” and 162.917” for the 10 m (1-6) and 6 m (7-15) antennas, respectively. Fits are clip
the 22% and 10% level for the 6.1 m and 10.4 m antennas, respectively. Typical imaging assumptions are such that the real component
size and amplitude beam size are identical, ellipticity is identically one and the imaginary component is negligible. The position angle
beam is expected to be near zero because the dish should fold top to bottom based on gravitational stresses resulting in an elongated be
the elevation direction. Uncertainties are the maximum of peak to peak divided by two or the standard deviation of the sample.

phase behavior in the pattern. Antenna 2 has, until very recently, had persistently high system temperature and thus poor sensitivity. Antenna 6 was often warm and was not present in many of the datasets. Antenna 7 had persistent phase jumps during this time and almost all of the datasets needed to be flagged.

Figure 2.23 shows an example of the real (left) and imaginary (right) voltage patterns over the range of observing parameters. The sets of three overlaid contours are from three distinct datasets. Some properties, e.g. ellipticity, are sufficiently small that they are not obvious in the datasets while others, such as the size and orientation of the imaginary beam, are clear and consistent over the various runs.

2.4.5.1 Frequency, Source and Sampling Dependence

In what follows all voltage pattern beam widths have been multiplied by the mean frequency of observation and divided by 100 to normalize all sizes to a 100 GHz. The difference in IF frequency has been accounted for in the first transform from sky to aperture plane, normalizing the patterns to the LO frequency. Most datasets were taken with a mean frequency of 100.2 GHz. However, the 10m and 6m each had a single dataset at a frequency 5 GHz different from the regular 100.2 GHz. In each case, the 5 GHz difference has no significant impact on the measured properties of the voltage pattern.

Most of the datasets were taken in CARMA's extremely compact, E-array, which has a resolution of ∼10.5" at 3mm. Mars (∼7.25" at time of observation) was often utilized as a 3mm source. First order amplitude scaling was removed by self-calibrating against a Mars model for all positions. Still, offset positions could in principle be affected by the finite size of the planet. In general, these effects should be minor as the typical baseline length used for the beam patterns is half the array size, or about 40 m. Mars is poorly resolved on such baselines. The expected irrelevance of a resolved Mars is echoed in the data with no discernible difference between values determined using the point sources 3c273 and 3c454.3 and those determined using Mars.

Finally, some of the datasets were taken with oversampling of the voltage pattern on the sky while others were taken in a roughly Nyquist sampled grid. Nyquist sampled patterns were taken as much larger patterns on the sky with the hope of deriving possible panel adjustment points and determining sidelobe properties and stability. On average, consistency was seen on most antennas. Pointing drift on the longer timescales required to obtain the larger patterns resulted in noticeable deviations for some antennas for some datasets. These antennas and datasets were not included in the final analysis. There is some hope that, in the future, optical offset guiding (Chapter **??**) can be integrated into the process providing longer timescales for pointing stability.

2.4.5.2 Beam Sizes

Beam sizes were fit in the same way as for the ensemble properties. Figures 2.24 (amplitude component) and 2.25 (real component) show the trends of voltage pattern size with elevation for the fifteen CARMA antennas. Each panel shows the voltage pattern size in arcseconds and the elevation plotted is the in degrees. The error bars in elevation indicate the range over which the data was collected. Error bars in beam size are the propagated errors in the original axis determinations. The dashed line provides an indication of the FWHM used by MIRIAD . Fits were clipped at the 10% level for the 10.4 m antennas and 22% for the 6.1 m antennas as the 10.4 m antennas contribute down to the 10% level for the heterogeneous baselines. In the future, the fits down to the 10% level for the 6.1 m antenna and 5% for the 10.4 m antennas will need to be considered as the SZA is included in CARMA.

In general, disagreement between the real and amplitude sizes (seen either in Figure 2.24 and 2.25 or Table 2.4) of the voltage pattern would indicate that there is significant imaginary component in the amplitude fit. A imaginary gradient, for example, would widen the beam in the direction of the gradient while having little effect on the orthogonal direction. Larger than expected amplitude patterns and amplitude only ellipticity would result. Shared deviations in the real and amplitude component or deviation of the real component alone are indicative of an overall error in the beam model. Such deviations could be as simple as focus error or perhaps something significantly more sinister.

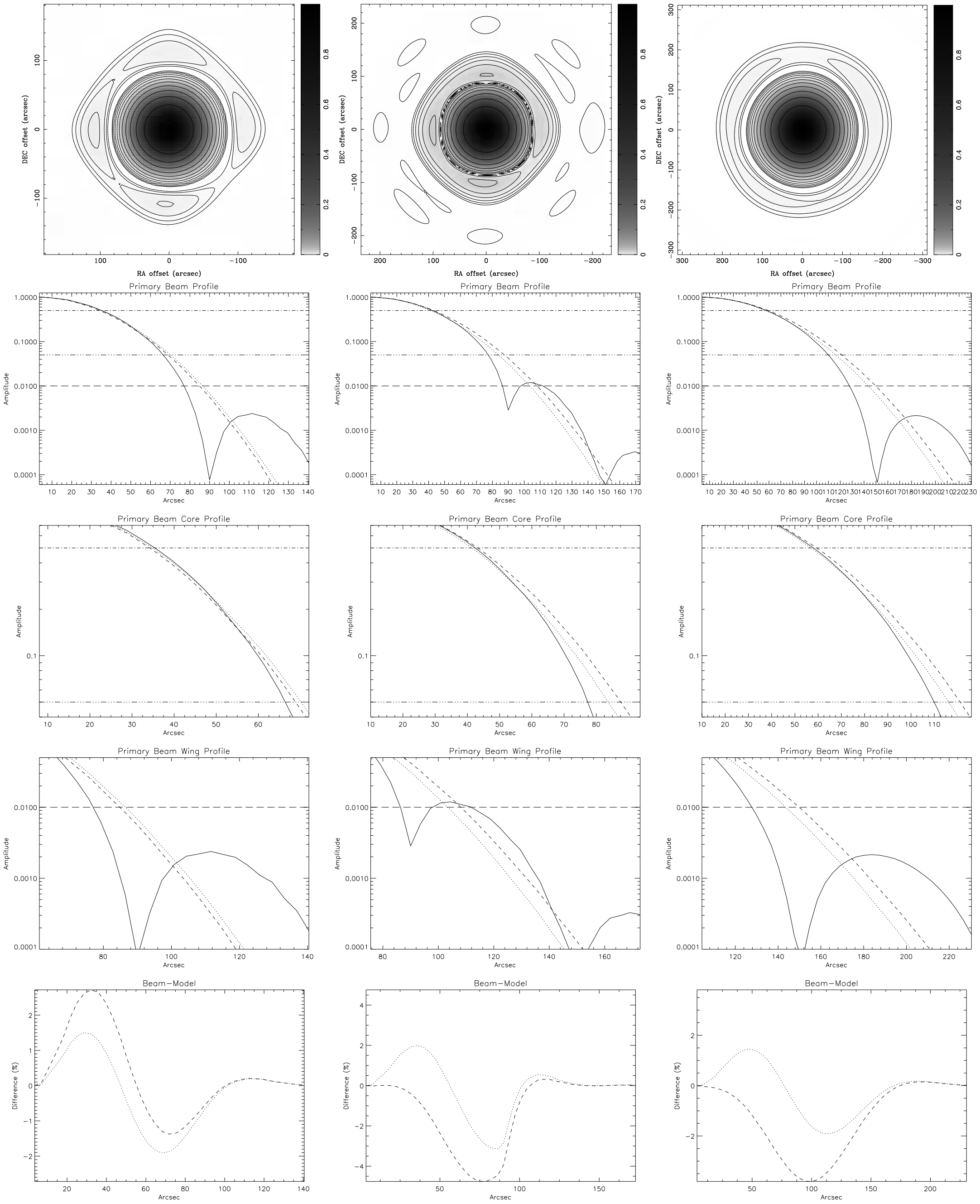

Figure 2.17 The top row shows the primary beam image for the 10.4 m, heterogeneous and 6.1 m baselines, respectively. The grey scale is log-stretch between 0 and 1. The contours peak at 90% and decrease by 2^n. The 5^{th} contour is approximately the 5% point. The lowest contours are ∼0.05% and are shown mostly to outline very faint features. The second row is the azimuthal average of the image directly above it plotted in log scale. The solid line is the data, the dashed line is the best-fit Gaussian and the dotted line is the model from MIRIAD. The horizontal lines are the half-power (dashed-dot), 5% (dashed-dot-dot) and 1% (dashed) points in the primary beam. The third row, again in log scale, zooms in on the half-power and 5% points in

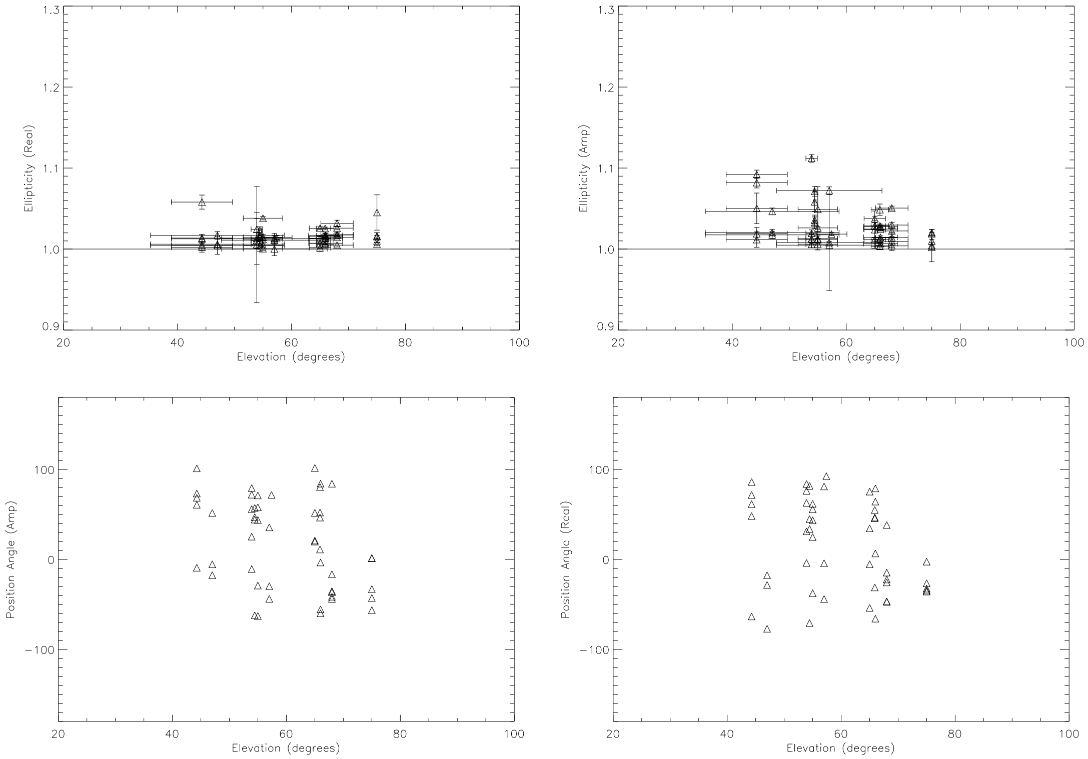

Figure 2.18 The real (left) and amplitude (right) voltage pattern ellipticity (top) and position angle (bottom) are plotted as a function of elevation. Data from C1-6 are included here. The horizontal axis is the elevation with error bars representing the range of elevation over which the data was collected. The vertical axis is the propagated error from the **imfit** fits to the axes.

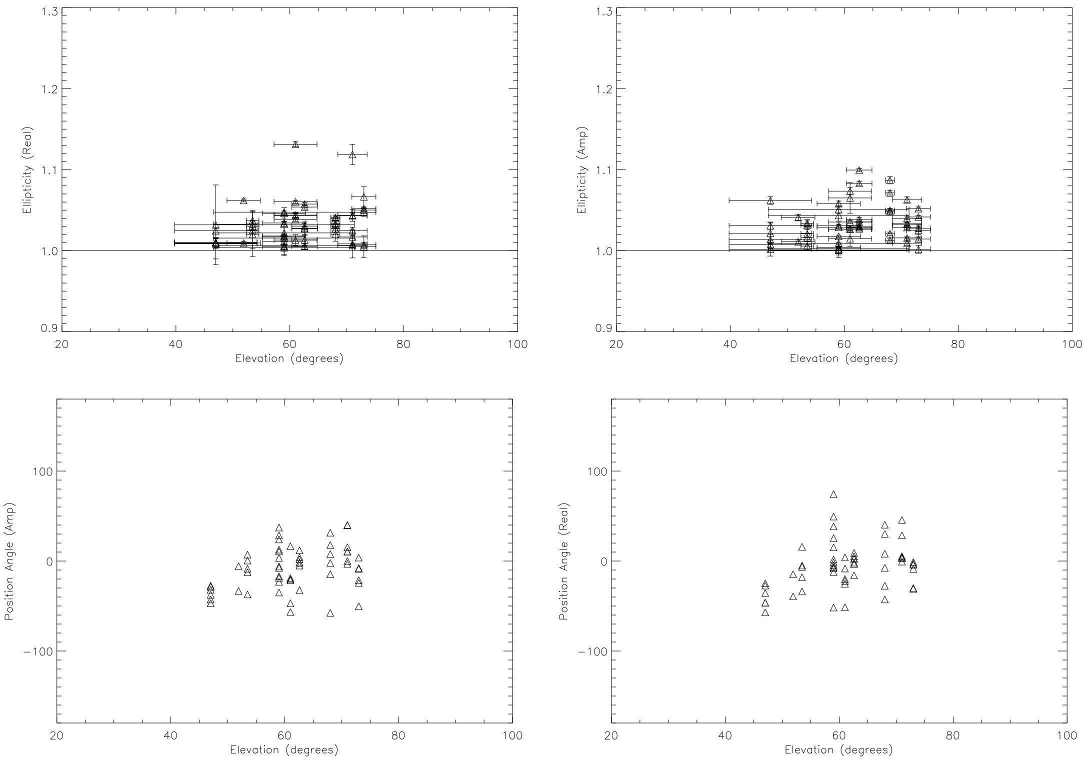

Figure 2.19 Similar to **??** except for the 6.1 m antennas.

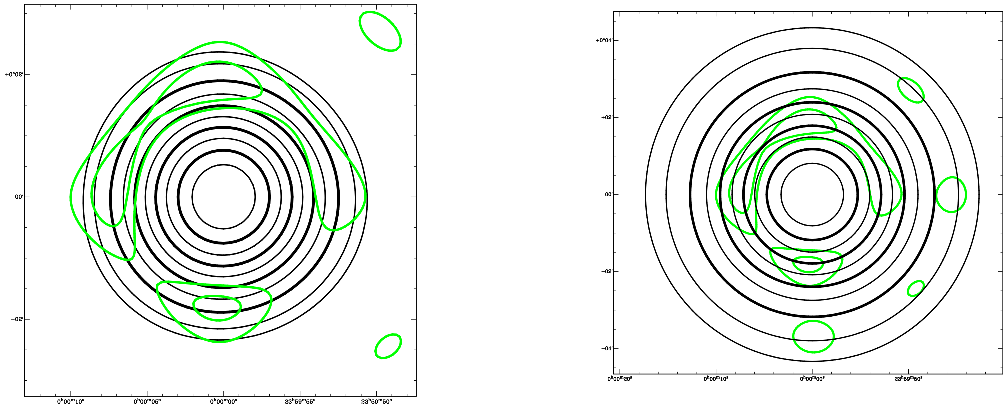

Figure 2.20 The left panel displays the negative, low-level sidelobes of the 10.4 m voltage pattern overlaid on the main beam of the 6.1 m antenna voltage pattern. The right panel shows the same but the main beam is that of a 3.5 m voltage pattern. The negative contours, shown in green, are -5% and -10% of the peak of the 10.4 m antenna voltage pattern. The black contours of the main beam are 5%, 10%, and then increasing by 10% up to 90% of the peak. When multiplied by the 6.1 m antenna voltage pattern, the peak 10.4 m voltage pattern sidelobes, ∼-13%, are multiplied by 0.25% resulting in 3% residual contribution which is significant in cases where the dynamic range needs to exceed about 100. On the right, the -13% sidelobes are now multiplied by 70% of the peak in the main beam giving 10% residual contribution which will be significant when the needed dynamic range is 30. A 6.1 m antenna voltage pattern overlaid on a 3.5 m antenna voltage pattern will look much like the left panel above given the proportions of the antenna sizes.

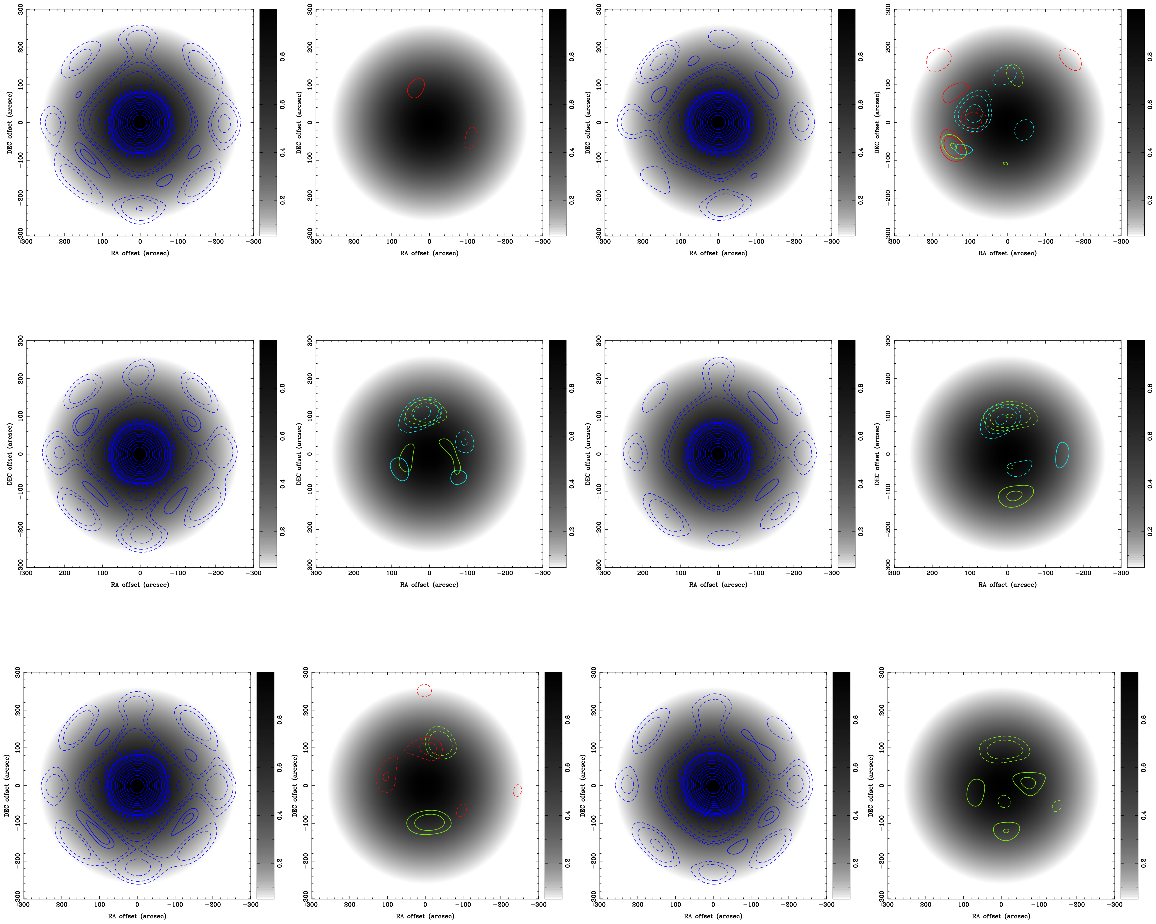

Figure 2.21 Real component voltage patterns for the 6 10.4 m antennas. The image is a model of the real voltage response of a 3.5 m antenna. The dark blue contours represent the six template images, one per antenna. Other datasets were subtracted from these template antennas and are show in red, cyan and green contours. In all cases except for C1 (top left of the figure) the green contours were taken close in time and on the same source as the template image whereas the red and cyan contours were taken close in time to each other and on a common source but at a time and on a source different than the template dataset. For C1, only two epochs were available. For this antenna, the template and red contours were from datasets taken close in time on the same source. The absence of contours indicates the absence of data, not a perfect fit. Contours are at 2%, 3%, 5%, 10%, 15%, 20%, and then increasing in 10% steps thereafter. Solid contours are positive and dashed contours are negative. The pair to the top left is for C1, top right is C2, middle left is C3, etc. The stability of a feature is best seen by noting the strength of the feature in the template image and then noting the variation, i.e. a sidelobe at 10% which has a 2% residual is 10±2%.

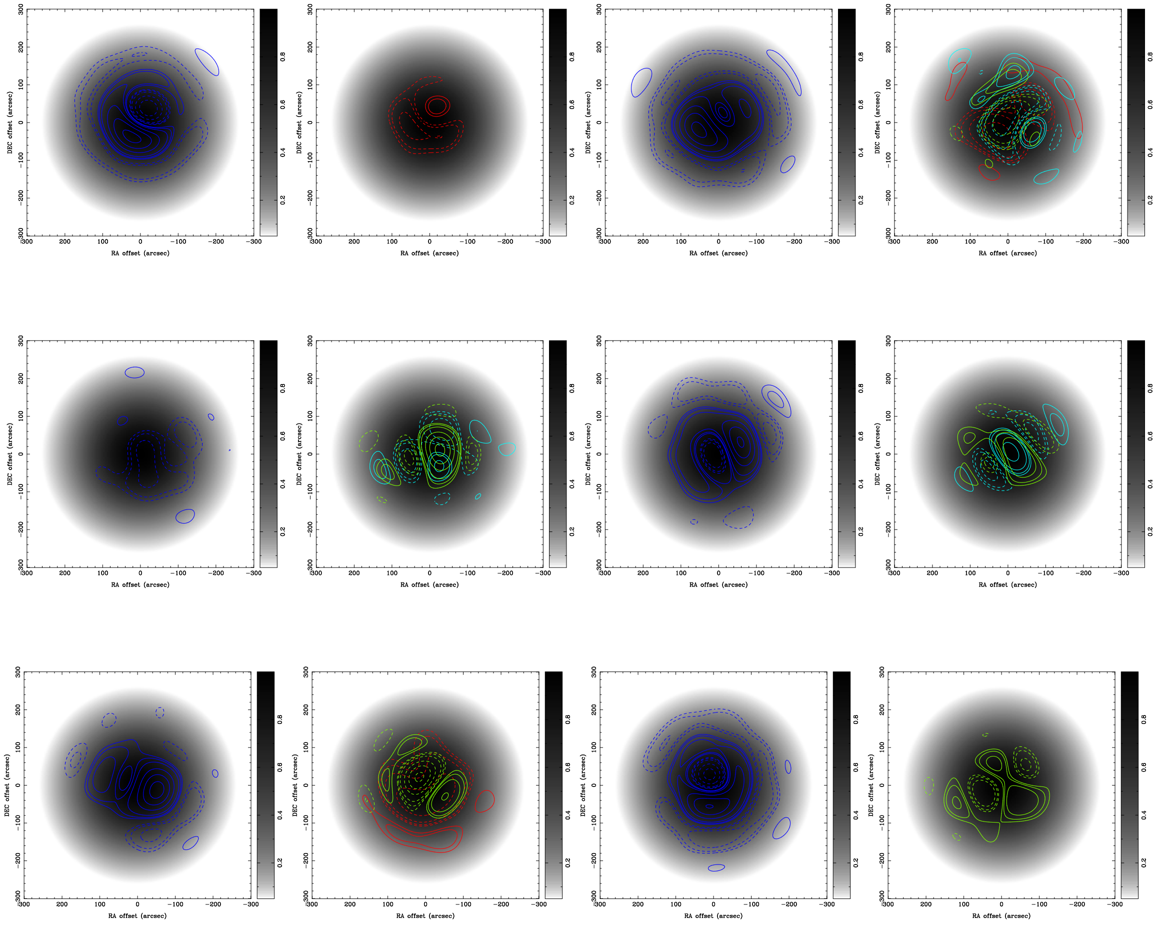

Figure 2.22 Same as 2.21 except for the imaginary component.

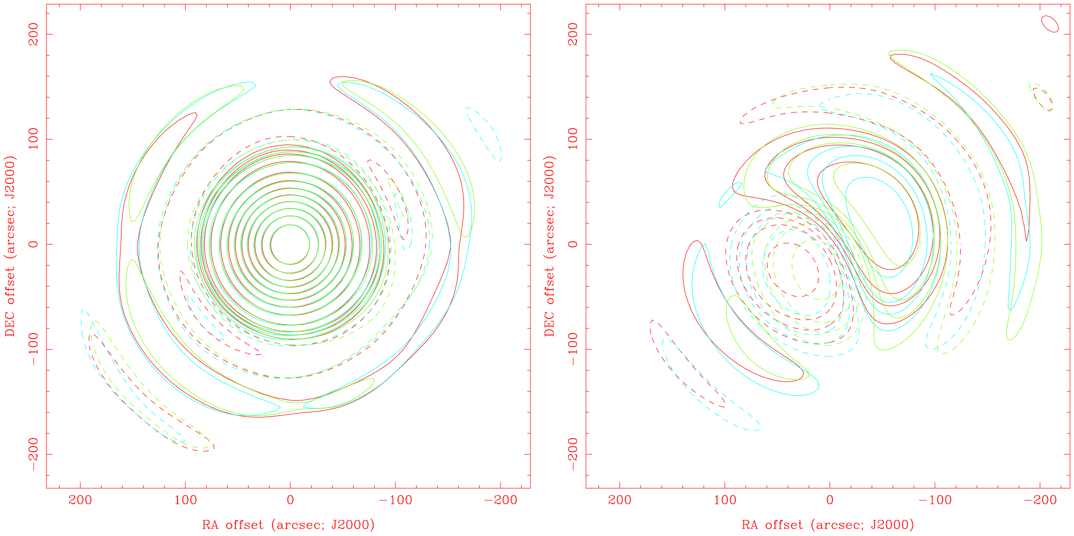

Figure 2.23 The real (left) and imaginary (right) voltage pattern is shown for C4 over three observing runs. Each run is highlighted in a different color with red, blue and green contours representing 2007-Sep-11 (two runs) and 2007-Sep-16. Dashed contours are negative structures while solid contours show positive features. The contours are 1%, 3%, 5%, 10%, then increasing at 10% intervals, normalized so that the amplitude has a peak of 1.

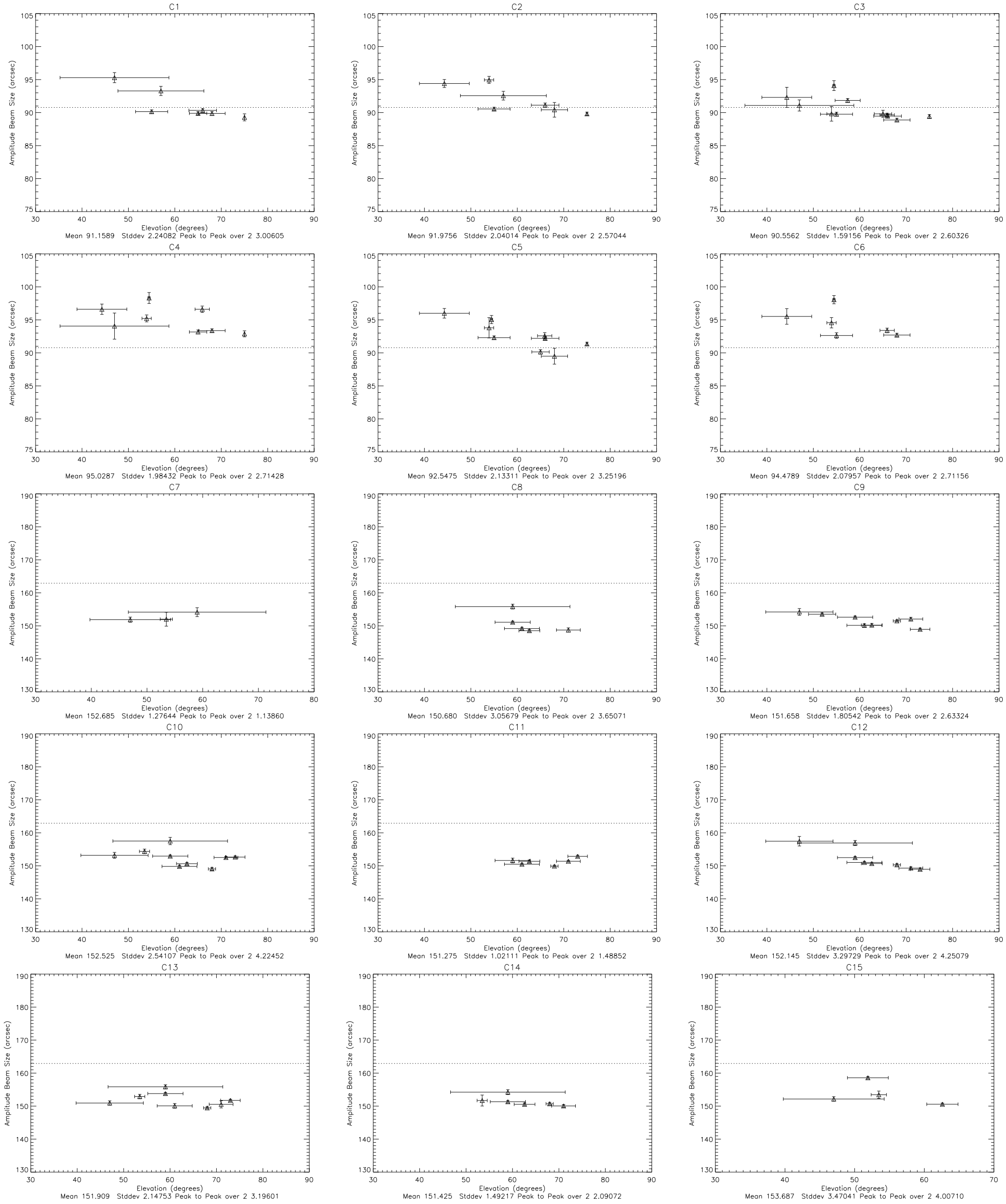

Figure 2.24 Each of the CARMA antenna amplitude voltage pattern widths is plotted against elevation. The horizontal error bars represent the range of elevations over which the data was taken. The vertical error bars are derived from the uncertainty in the original fit parameters.

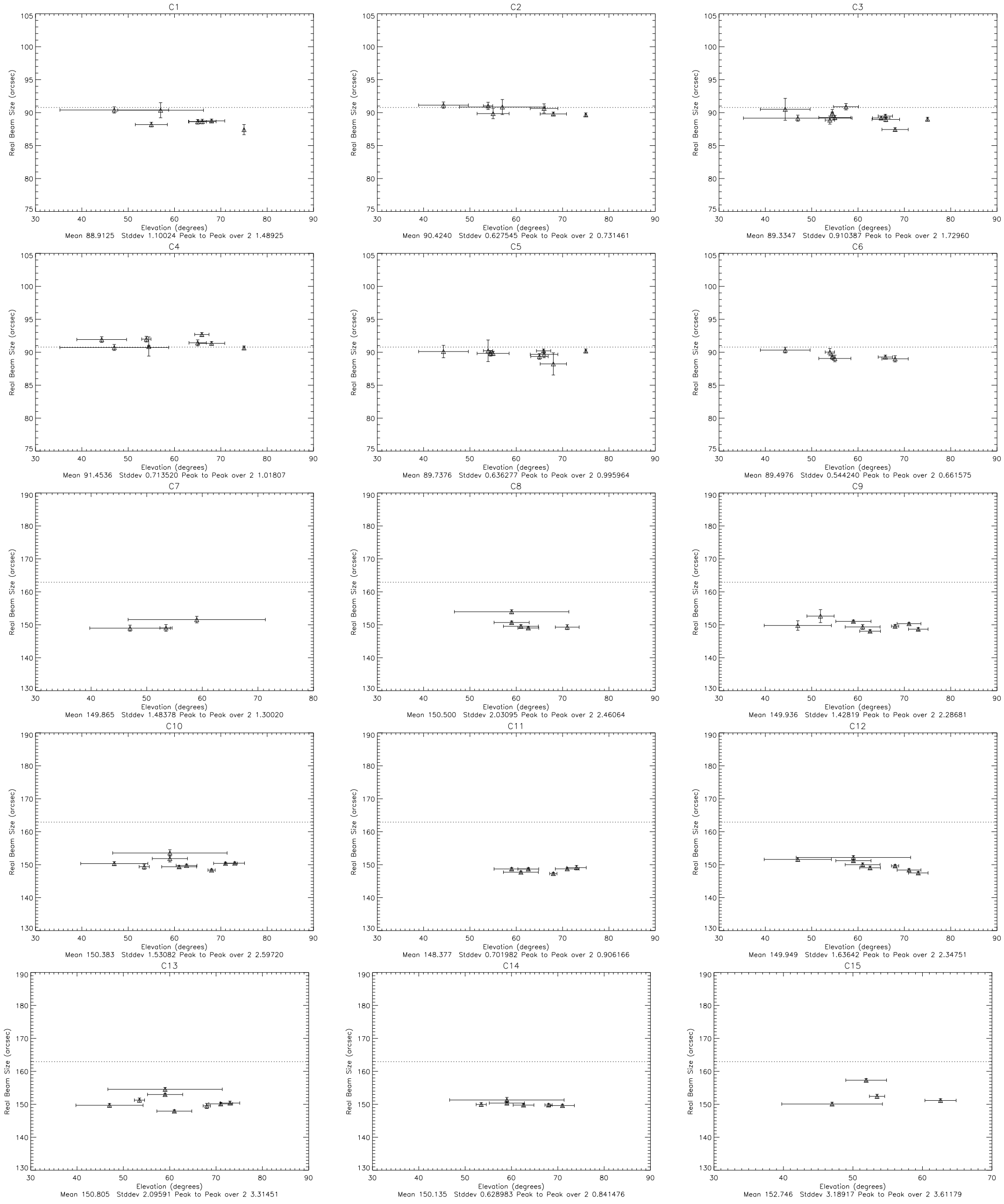

Figure 2.25 Same as Figure 2.24 except the fit to the real component of the voltage pattern is plotted.

Several of the 10.4 m antennas (C1, C2, C5) show evidence of variation in amplitude voltage pattern size as a function of elevation. C6 also However, the same trend is *not* seen in the real components. This most likely, again, implicates the contribution of the imaginary component. The sag of the secondary as a function of elevation can change the illumination of the primary. This would effect only the size of the amplitude ellipticity and/or beam size but would not effect the real component. In addition to the principle axis focus control available on both the 6.1 and 10.4 m antennas, the 10.4 m antennas have the capability to change the position of the secondary with respect to the principle axis and this problem could be rectified. The more stiff 6.1 m antennas show no such evolution and have strong agreement between the real and amplitude component in general, indicating that any imaginary component, if present, is at a low level.

Of the 10.4 m antennas, only C4 shows any significant deviation in the real pattern size with the balance of the antennas showing remarkable agreement with the FWHM given by MIRIAD. The most likely source of the deviation of C4 is a focus error. Indeed, quadratic fits to the phase pattern in the aperture plane reveal this antenna typically has a factor of two larger contribution than its normal sized counterparts for the runs in question. Proper adjustment of the antenna focus will likely return the real component of C4 to the nominal value for the other antennas. For the 6.1 m antennas, all of the difference is accounted for by the aforementioned difference between the ensemble properties of the 6.1 m antennas and the values in MIRIAD.

2.4.5.3 Ellipticity & Position Angle

Ellipticity was calculated as described above. Figures 2.26 and 2.27 show the trends of the amplitude and real component ellipticity as a function of elevation for the fifteen CARMA antennas. A dashed line is provided at an ellipticity of 1, i.e. circularly symmetric, for reference. Figures 2.28 and 2.29 show similar plots for the position angle of the ellipticity.

In general, one might expect the position angle of the real component ellipticity to be near zero while the amplitude ellipticity could mirror the real component or vary due to imaginary contributions. The real and amplitude based ellipticity should either be comparable or the amplitude ellipticity should be larger. Contribution to the ellipticity of the amplitude pattern can come from either inherent beam elongation or imaginary components whereas the real component should only be susceptible to elongation due to dish structure. In order for a definitive assignment of ellipticity to be made, the position angle should be roughly consistent trial by trial or have some definitive behavior as a function of elevation.

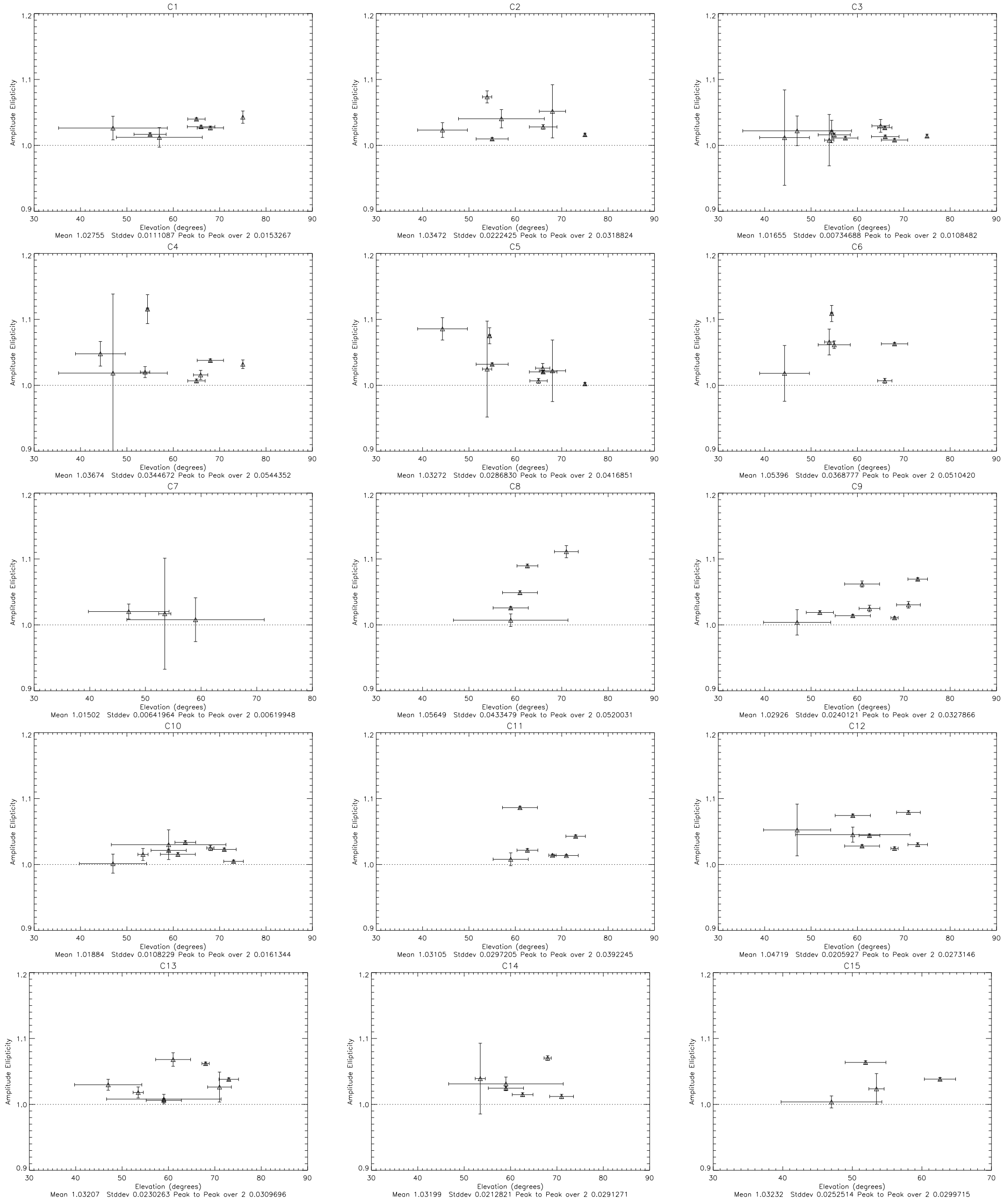

Figure 2.26 Each of the CARMA antenna amplitude ellipticity is plotted against elevation. The horizontal error bars represent the range of elevations over which the data was taken. The vertical error bars are derived from the uncertainty in the original fit parameters. The dashed line is an ellipticity of 1, i.e. circularly symmetric.

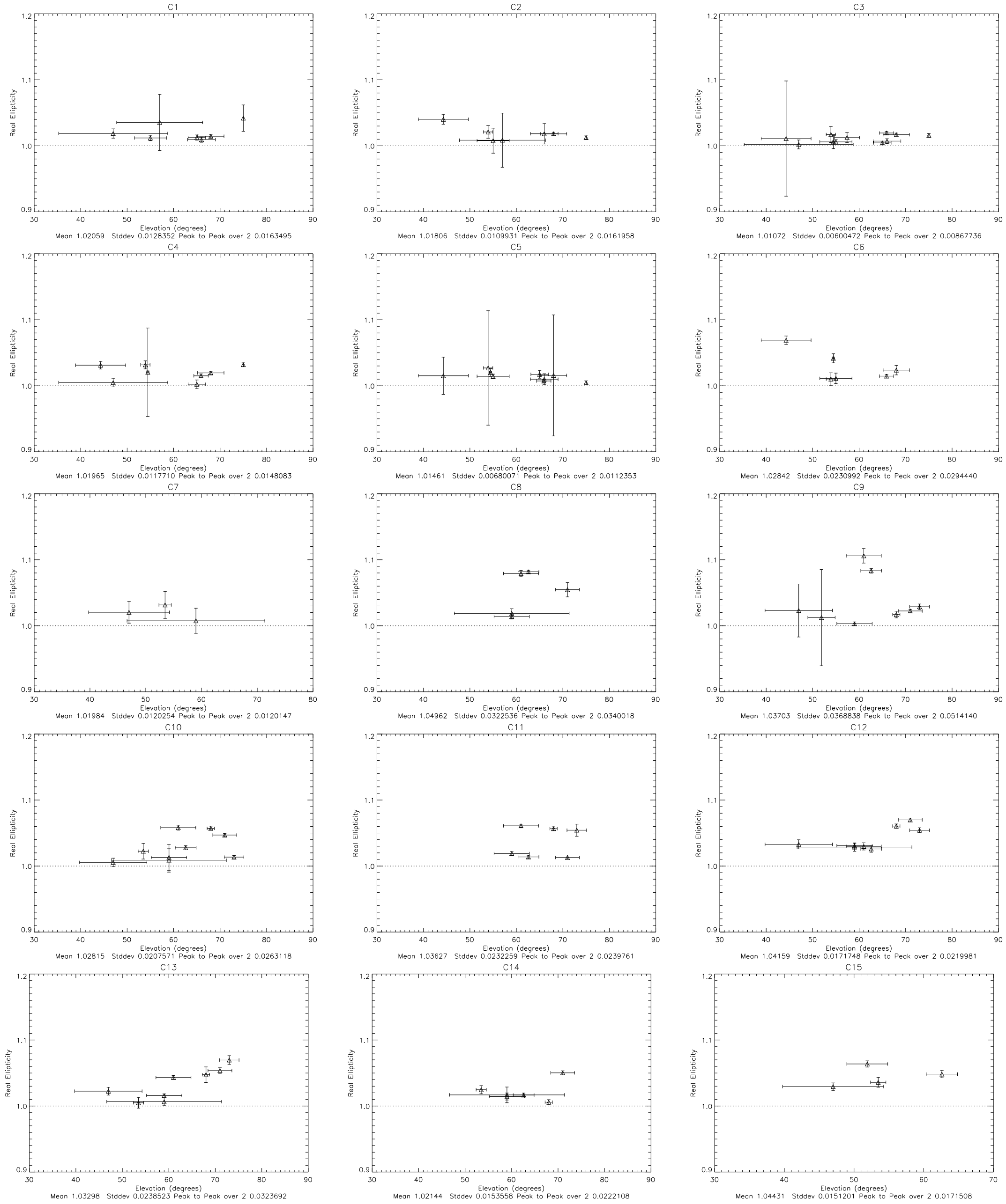

Figure 2.27 Same as Figure 2.26 except the fit to the real component of the voltage pattern is plotted.

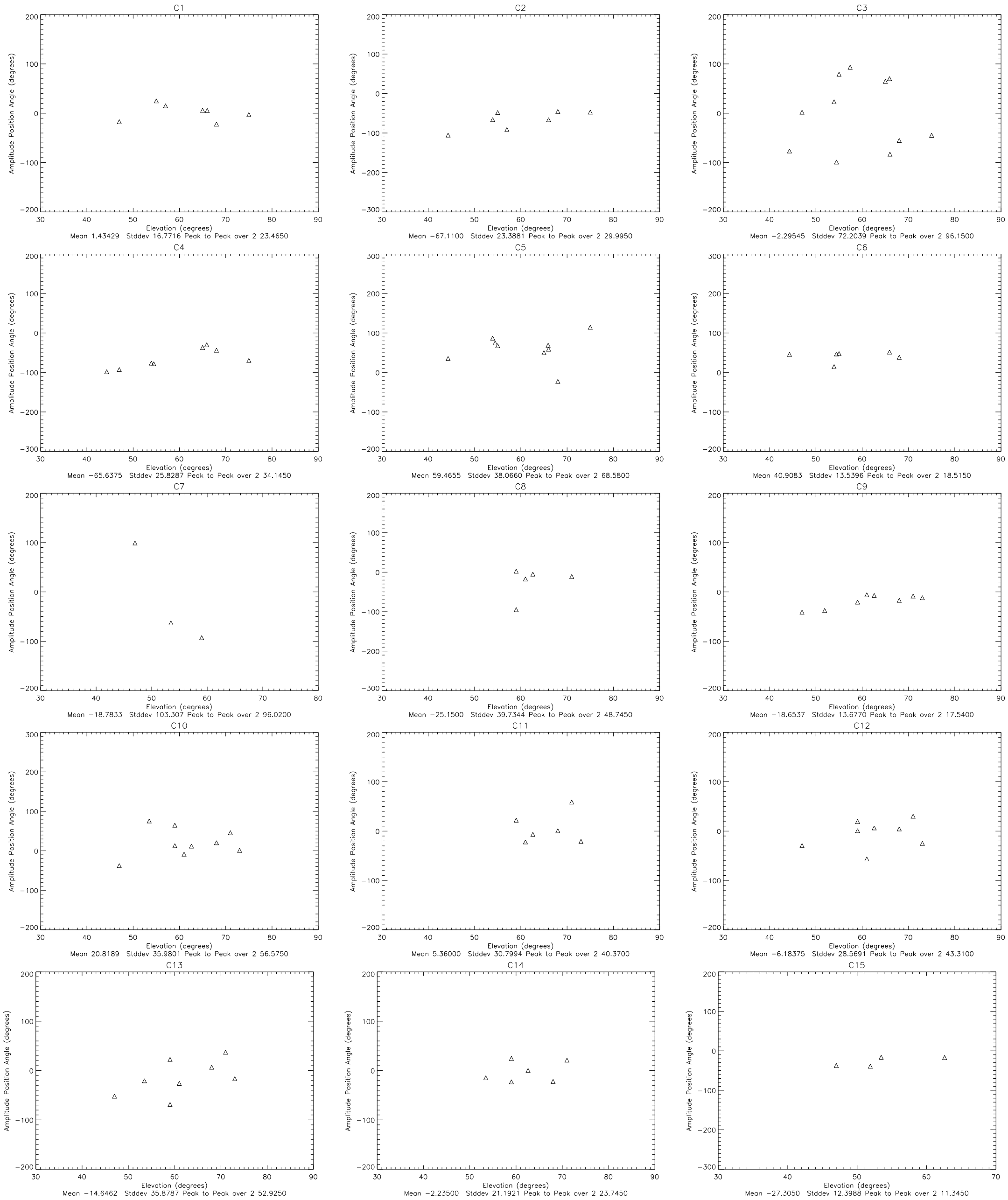

Figure 2.28 Plots position angle of the ellipticity amplitude voltage pattern as a function of elevation for the various antennas.

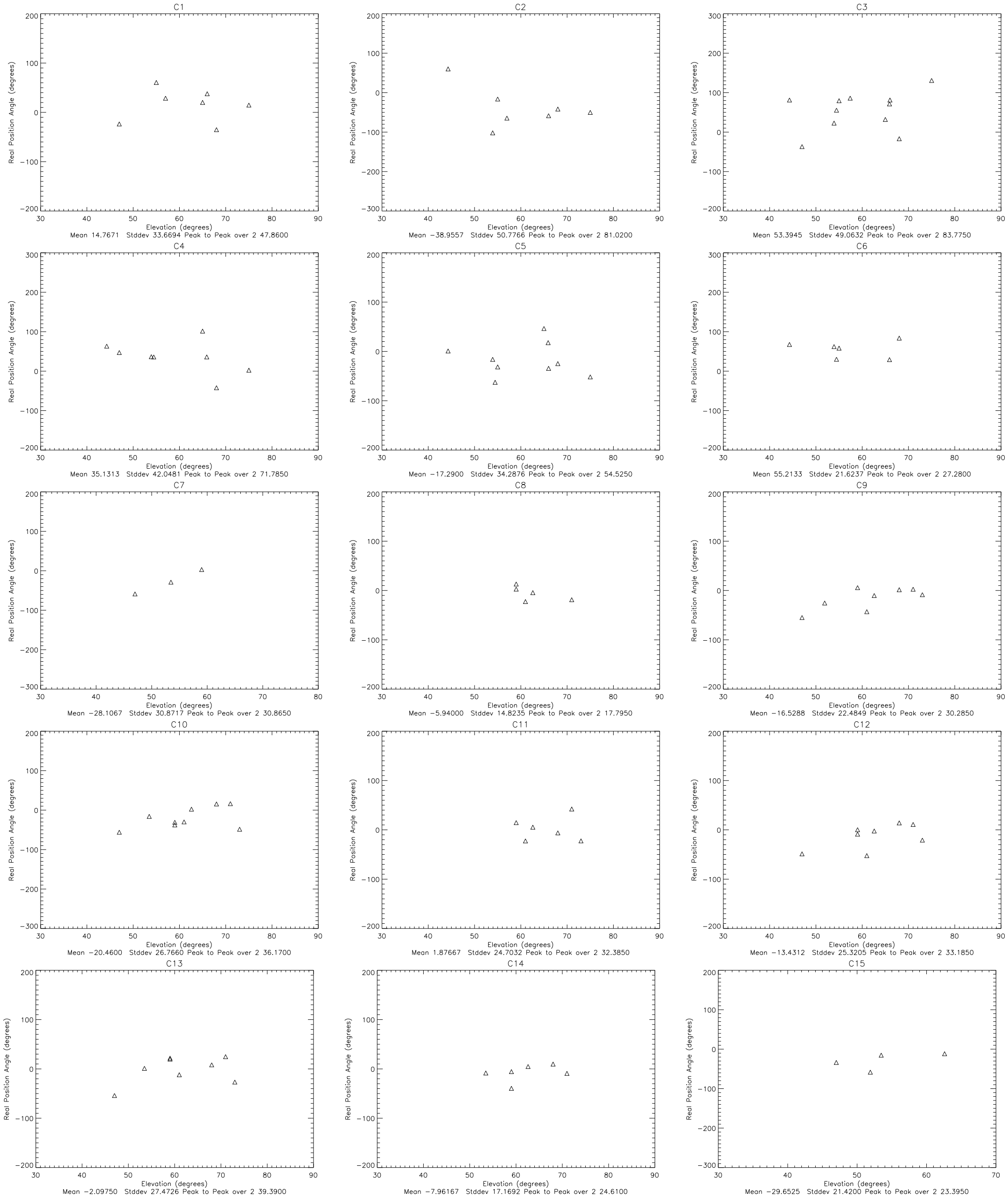

Figure 2.29 Same as Figure 2.28 except the fit to the real component of the voltage pattern is plotted.

Few of the 10m telescopes show signatures of true ellipticity where true ellipticity is contrasted here with ellipticity induced by the presence of an imaginary beam. C1 (top left panel of 2.26 through 2.29) has a persistent measure of ellipticity and a position angle consistent with zero. In the mean the ellipticity is 2.8±0.4% for the amplitude pattern and 2.1±0.3 for the real pattern. These have position angles of 15±13 and 1±7, respectively. The ellipticities and position angles are consistent within 2σ and 1σ, respectively. None of the other 10.4 m antennas show evidence of consistency between the real and amplitude ellipticity or position angle. There is no obvious trend of ellipticity or position angle with elevation a trend which repeats itself for most antennas with the exception amplitude ellipticity of C5. This antenna has far larger amplitude ellipticity than real ellipticity, suggesting that the evolution may be evolution in the illumination pattern on the antennas surface than inherent to the antenna.

The 6.1 m antennas showed consistent, 3% ellipticity as an ensemble. Table 2.4 and figures 2.26 through 2.29 indicate that for a given antenna the ellipticity derived for the real and amplitude components agree easily within the spread. The variation of ellipticity from antenna to antenna is not large and any evidence of departure from the ensemble property comes from antennas which have very few datasets.

2.4.5.4 Imaginary Beams

In the introduction, I show how offsets in the aperture plane result in imaginary beams across the sky via a simple simulation and application of the Fourier transform shift theorem. Figures 2.30 and 2.31, as well as Table **??**, show the half peak to peak of the imaginary components and position angle of that imaginary component, respectively. The magnitude of the imaginary beam can be interpreted as a percentage of the contribution to a completely real beam. A value of 0.1 implies that one quadrant of the beam will receive a positive, 10% imaginary contribution relative to the beam peak while the opposite quadrant will receive the same, but negative contribution. For the imaginary beam to be interpreted as believable, consistency of the magnitude of the peak to peak value and the position angle are required. Here, unlike the ellipticity, the position angle does not have a preferred direction and has no 180° symmetry. An additional constraint is applied by considering the magnitude of the real beam actually at the location of the peak imaginary component. If the peak imaginary component occurs at the 10% point of the real beam the phase error will be large the the contribution to the measured visibility will be small.

In general, contributions to the imaginary beam should arise from phase noise in the measurement of the beam on the sky. Some filtering is done by first transforming to the aperture plane, clipping emission beyond the aperture, padding the image with zero and transforming back. This removes much of the spurious imaginary signal that can exist in the sky only data and provides interpolation in the sky plane.

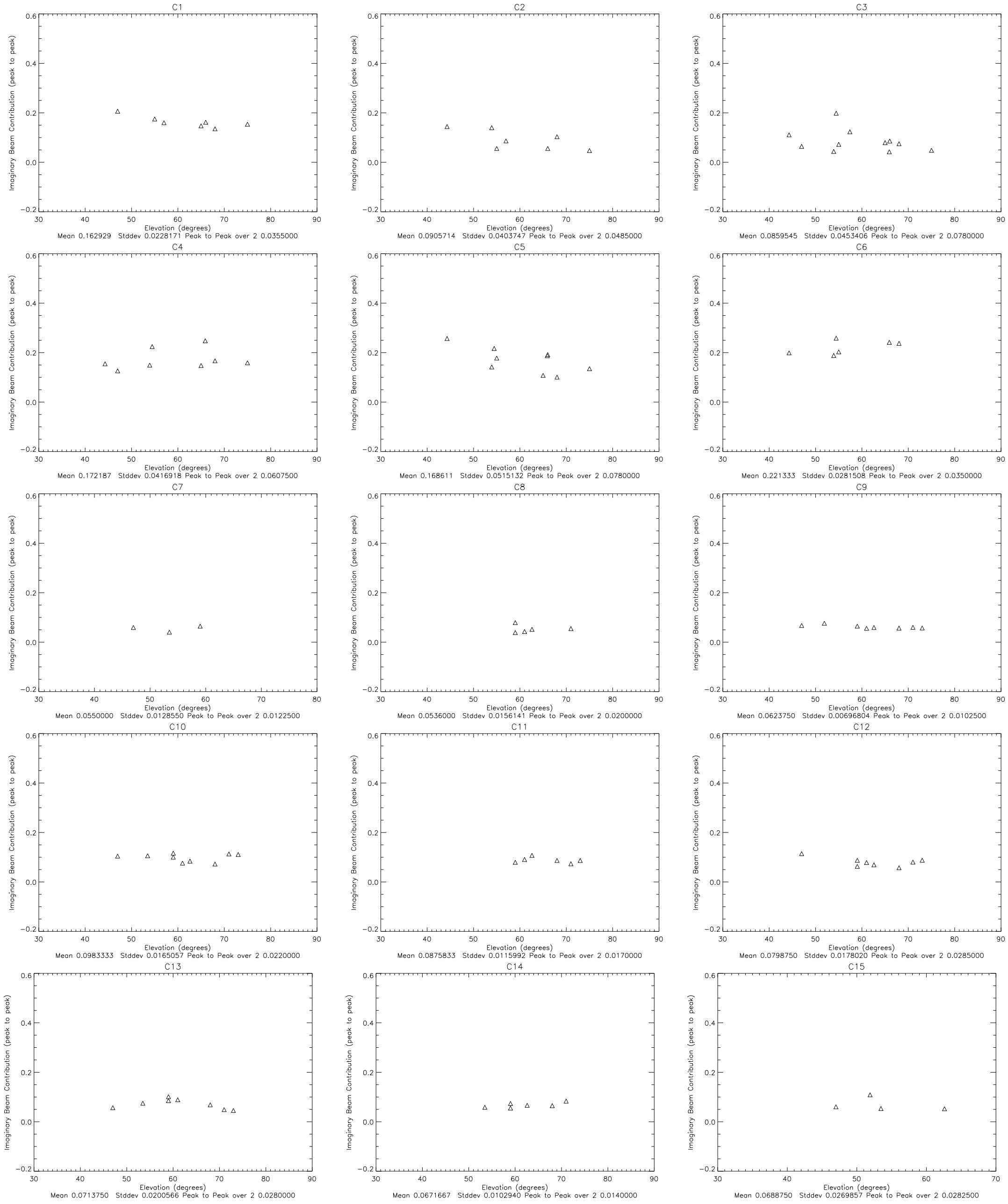

Figure 2.30 The magnitude of the imaginary component of voltage pattern for each of the 15 CARMA antennas is plotted against elevation.

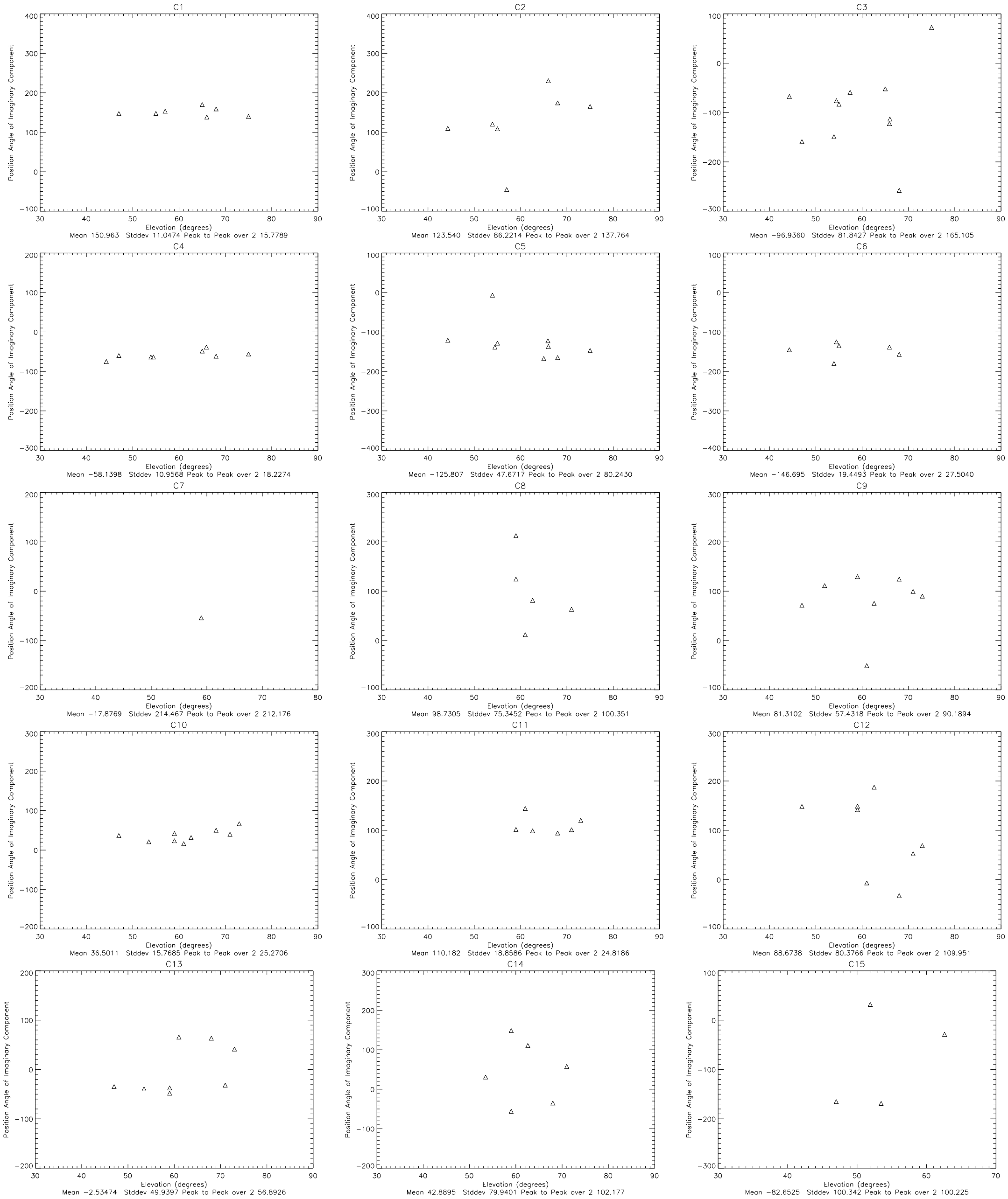

Figure 2.31 The position angle of the imaginary component of the voltage pattern for each of the 15 CARMA antennas is plotted as a function of elevation.

Given the principle contribution to the imaginary beam is an offset in the illumination pattern, I expect little consistency between the ensemble of antennas for any style of antenna. There are a variety of adjustment points for the 10m antenna alignment though ideal alignment is difficult. Indeed this is the case and a uniform model of the imaginary beam could not be constructed for either antenna style. One could envision a situation where the presence of feedlegs and other circular symmetry breaking components could result in uniform phase contributions but CARMA does not see such deviations at the level of repeatability of these measurements.

Several 10m antennas show very compelling evidence of imaginary beam contributions. C1, 4, 5 and 6 show small scatter in the peak to peak value and the position angle of the imaginary component. Considering deviations of the mean the relevant values are 0.163±0.009 151°±4°, 0.172±0.016 -58°±4°, 0.169±0.018 -141°±7°, and 0.221±0.013 -147°±9° for C1, 4 5, and 6, respectively. In each instance, the average location of these peaks is above the 50% point in the real beam. C2 and C3 have very low peak-to-peak values and nearly 90° uncertainty in the position angle of the imaginary component. Given this would include all possible angles at 2-3σ and the contribution comes at <40% in the real beam leaves little doubt that these gradients are not real.

Of the 6m antennas, only C10 and C11 show consistent evidence of a imaginary component as the scatter in the position angles is far too great in the other antennas to be interpreted as an actual gradient. The components are 0.098±0.006 37±6° and 0.088±0.005 110±8° for C10 and C11, respectively. The peak imaginary component for C10 comes at the 46% point in the real beam while the C11 component comes at a much lower level, 27%.

The contributions from the 6.1 m antennas are far less worrisome in the short term as these imaginary components are multiplied by the 46 and 27% point in the beam of other 6.1 m antennas and at the $\leq$10% of the 10.4 m antennas and are thus surpressed in 6.1 m cross 6.1 m baselines and strongly suppressed in heterogeneous baselines. For CARMA-23 this will no longer be the case. For the 10.4 m antennas, the contribution is far more serious. The 50% point of the 10.4 m voltage pattern is at the 80% point of the 6.1 m voltage pattern and these imaginary components are not strongly suppressed. CARMA-23 will only make this problem worse.

2.4.5.5 Antenna Based Templates: 2006Aug-2008May?

In the end, when maximal image fidelity is needed, a given array of N elements needs to be treated as a heterogeneous array with N real voltage patterns and N imaginary voltage patterns. The degree of variation seen in the antenna based properties re-enforces this concept at CARMA. This is a departure from how all imaging software, treats the situation. In MIRIAD, the heterogeneous aspects of the array are treated by the number of distinct baseline types, three in the case of CARMA (six for CARMA-23). In the approach taken here, the voltage pattern of antenna **A** must be multiplied in a complex sense by the conjugate of the voltage for antenna **B** to create a baseline based primary beam. In general, it is better to rely on the voltage patterns as this is the minimal number of independent images needed to produce the full array and it allows for pointing errors to be introduced or corrected post-processing on an antenna basis, which is the way in which pointing error is actually introduced.

Figures 2.32 through 2.46 display the final, 3mm, voltage patterns for use with observations over the shared risk period and first full observing season at CARMA and into the second season. The patterns are available for public use at:
cedarflat.mmarray.org/holography/templateVoltagePatterns/
under the names a#.s.real and a#.s.imag. These patterns are expected to change and must be re-measured upon alteration of focus properties, adjustment of panels or alignment of optics. (See the README file at the same webpage for information about the time applicability ranges of these patterns.) The patterns shown here are unique to 100.2 GHz observations. These patterns can be scaled to any 3mm frequency by utilizing the python wrapper **alterFreq.py** provided on the webpage. The required inputs are desired frequency and an identifier for the output directory. The output files are called a#.s.freq.real and a#.s.freq.imag and are placed in a subdirectory with the same name as the provided identifier. The command structure is quite simple and is a repeated call to MIRIAD tasks **puthd** and **regrid**. (See the

same README file for running instructions or cshell equivalents.) In general, the patterns must be rotated to various parallactic angles to be applied to simulated or measured data. See Chapter 1 for information regarding publicly available routines to apply these beams to simulated data or Chapter 3 for applications to real data.

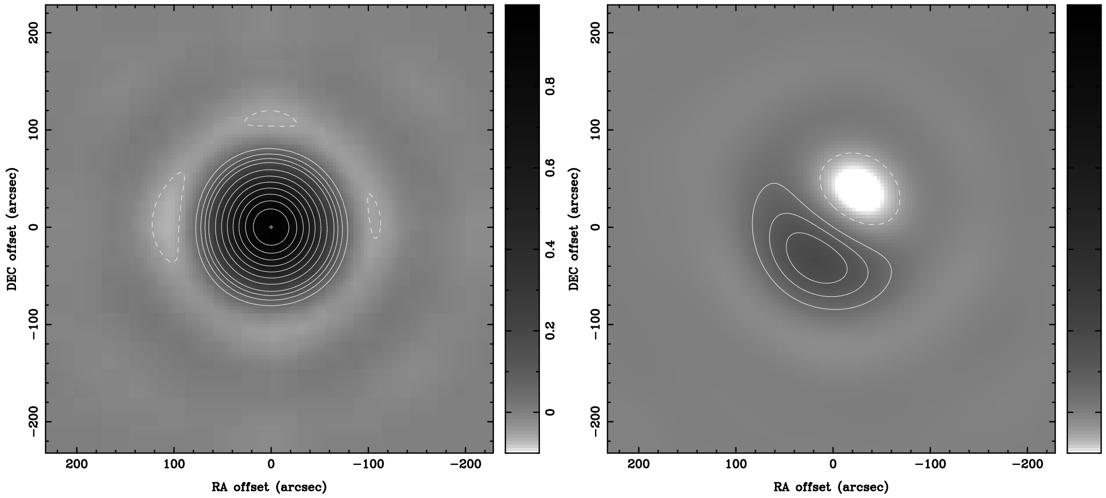

Figure 2.32 The real (left) and imaginary (right) mean voltage pattern at 100.2 GHz is shown for antenna C1. The image stretch is log ranging from -10% to 100%. The contours are drawn at 5% intervals until 20%, increasing in 10% intervals thereafter with dashed contours negative and solid contours positive.

2.5 Summary & Conclusions

There were two goals of this work. First, the properties of the antennas were to be optimized. To this end, I have optimized the surfaces of the 6 m antennas and aided in the optical alignment of the 10 m antennas. There are surface improvements which could be made to the 10 m antennas based on the repeatability of the holography but the surface RMS is within tolerable limits unless 850μm receivers are installed. I have determined that the alignment of the 10 m antennas at 1mm is poor and the alignment process is now underway. No credible dataset is available to assess

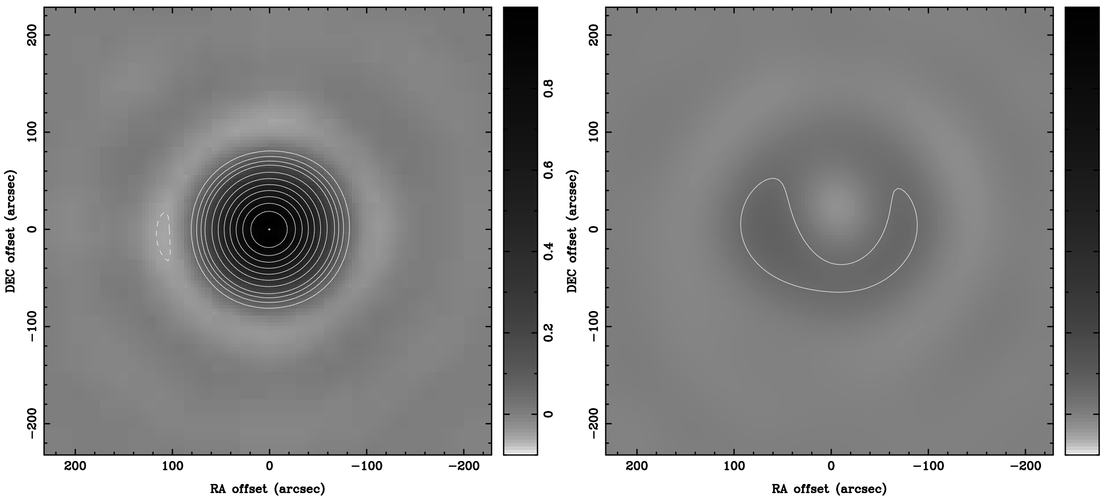

Figure 2.33 Similar to 2.32 but for antenna C2.

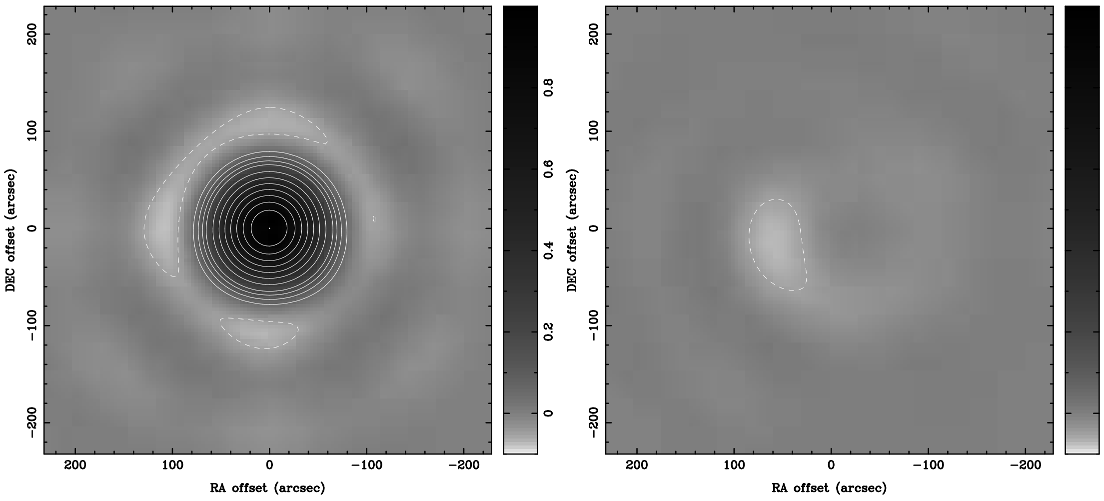

Figure 2.34 Similar to 2.32 but for antenna C3.

the alignment of the 6 m antenna at 1mm. A single adjustment of C3 at 1mm was made and the results indicate that the alignment is dramatically improved over that shown in Figure 2.12. The alignment and surface RMS post- adjustment are listed

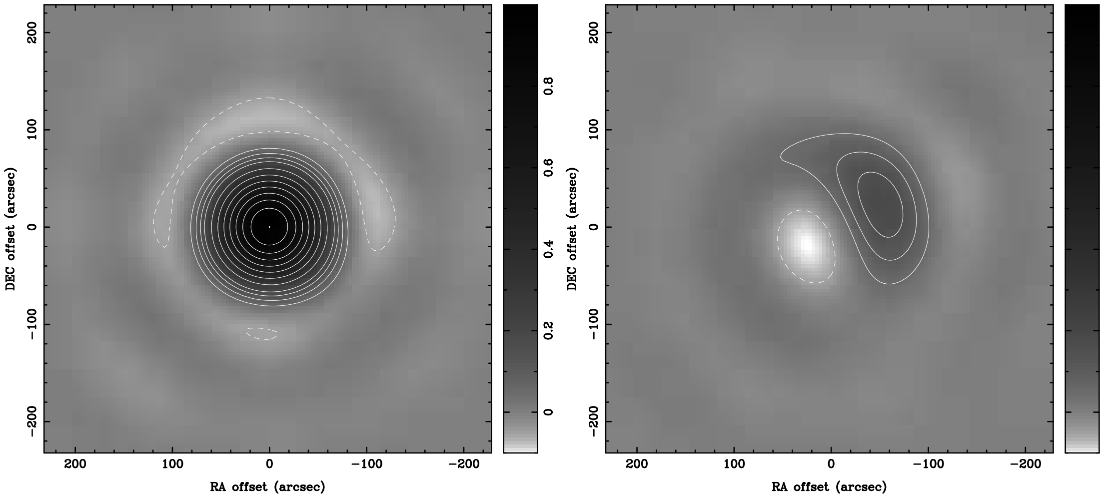

Figure 2.35 Similar to 2.32 but for antenna C4.

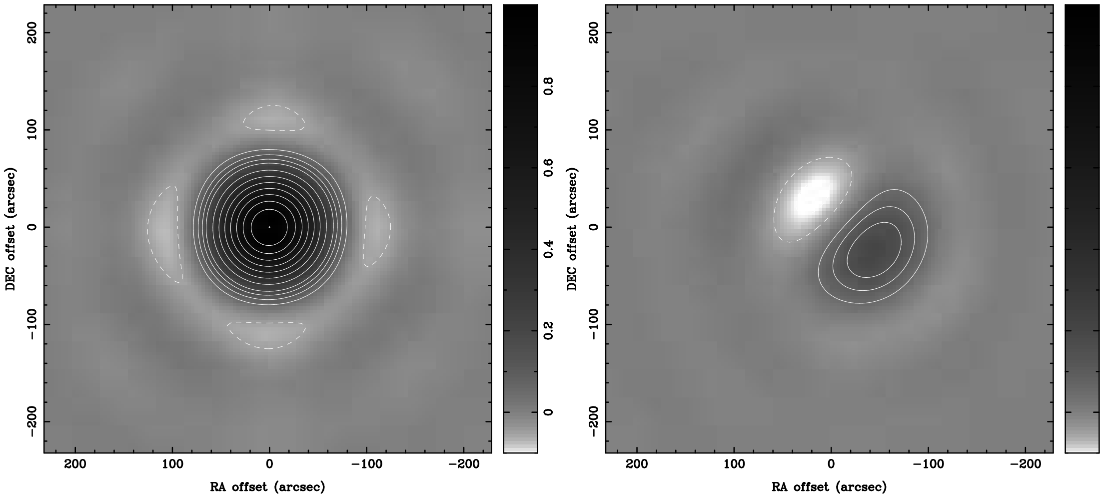

Figure 2.36 Similar to 2.32 but for antenna C5.

in Table 2.2. There are several instances of large alignment offset though all of the antennas are at or near the benchmark for surface accuracy.

The second goal was to measure the empirical voltage patterns and provide:

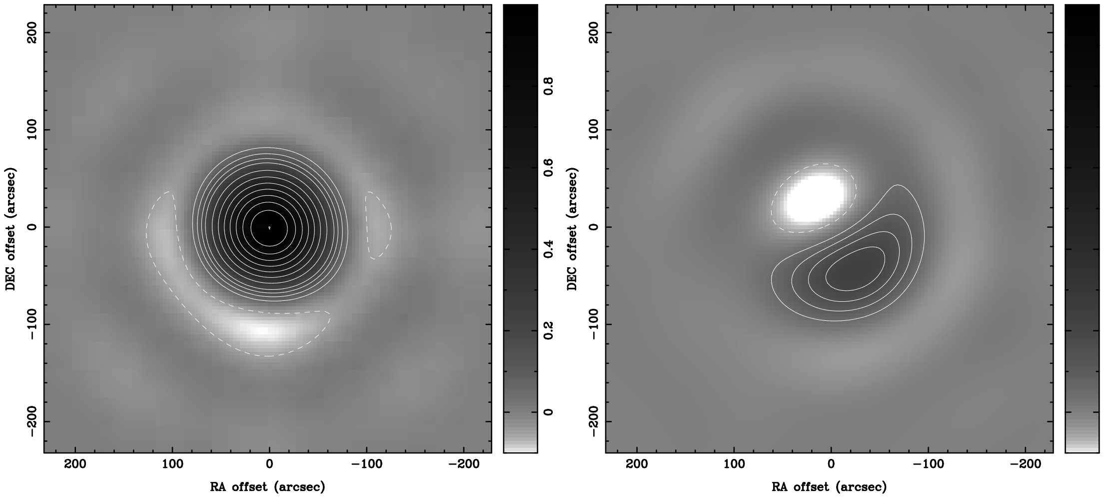

Figure 2.37 Similar to 2.32 but for antenna C6.

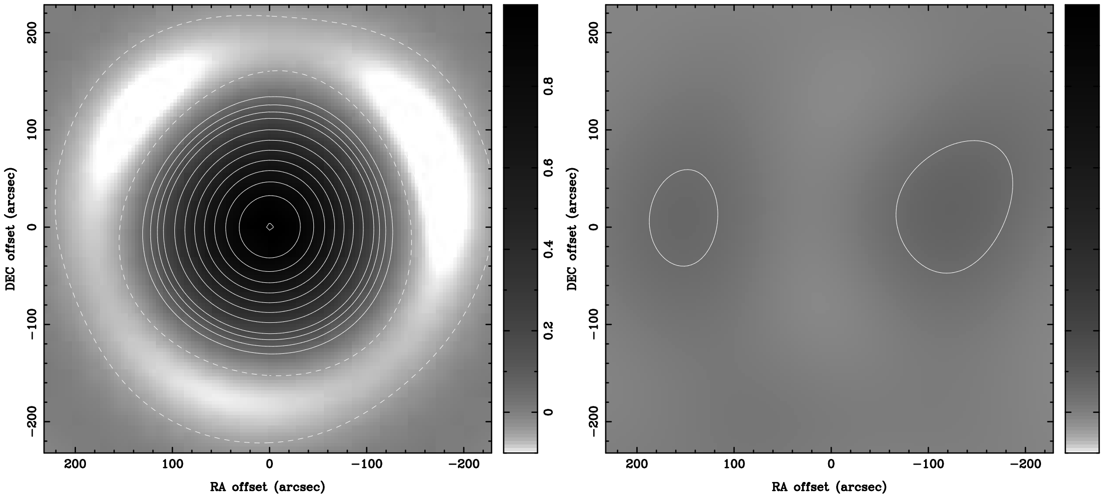

Figure 2.38 Similar to 2.32 but for antenna C6.5

- **A better estimate of the width of the symmetric, Gaussian approximation used for the 6.1 m, 10.4 m and heterogeneous primary beams for immediate integration into MIRIAD.**

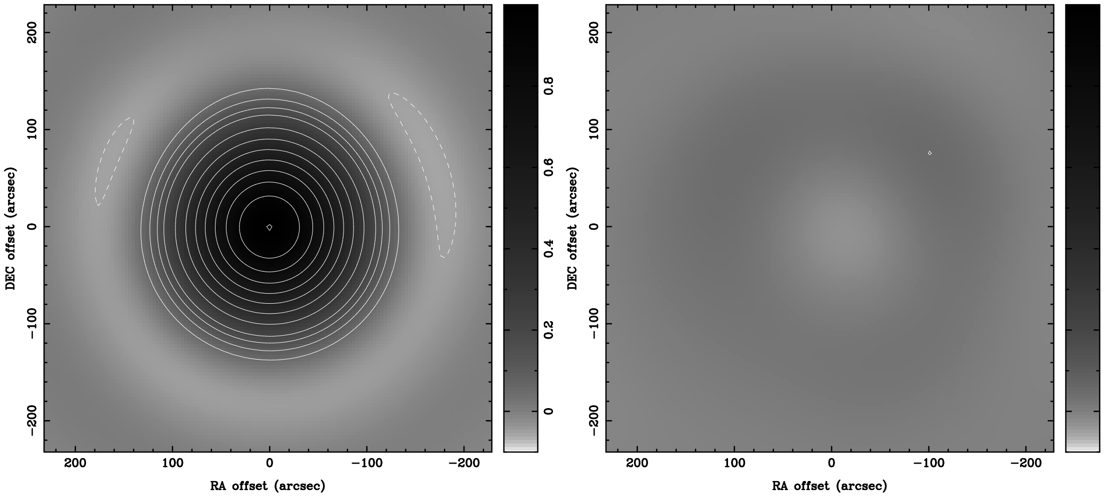

Figure 2.39 Similar to 2.32 but for antenna C8.

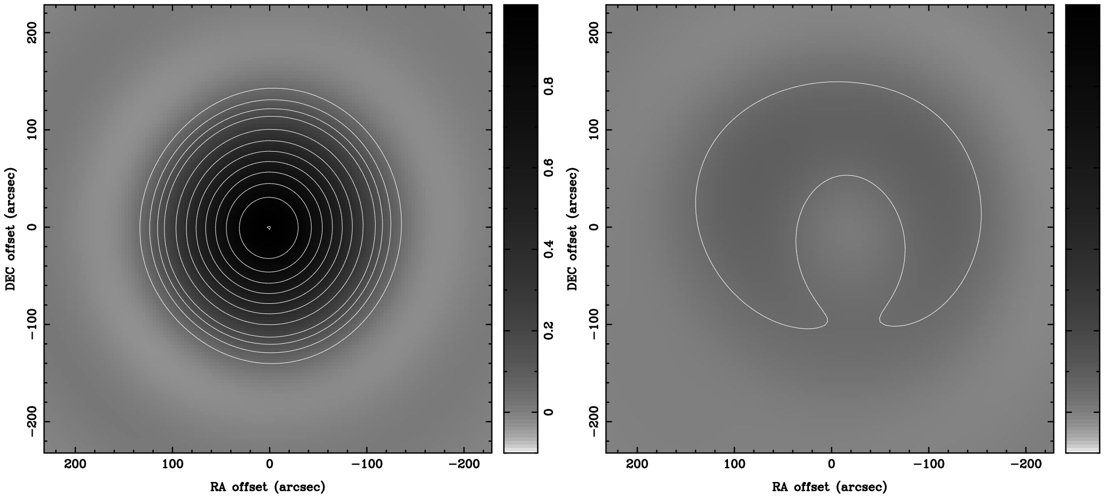

Figure 2.40 Similar to 2.32 but for antenna C9.

- **An estimate of the deviation from the symmetric, Gaussian approximation**

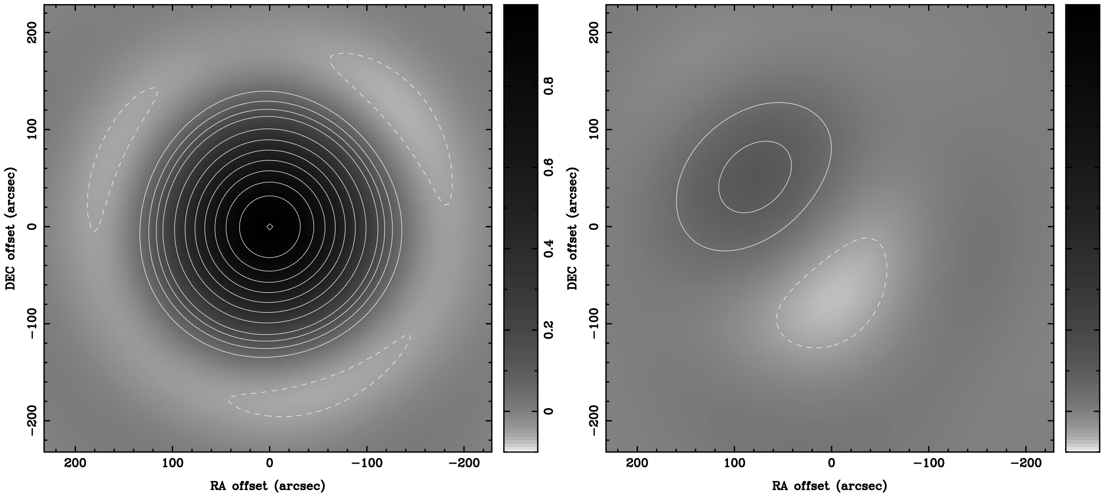

Figure 2.41 Similar to 2.32 but for antenna C10.

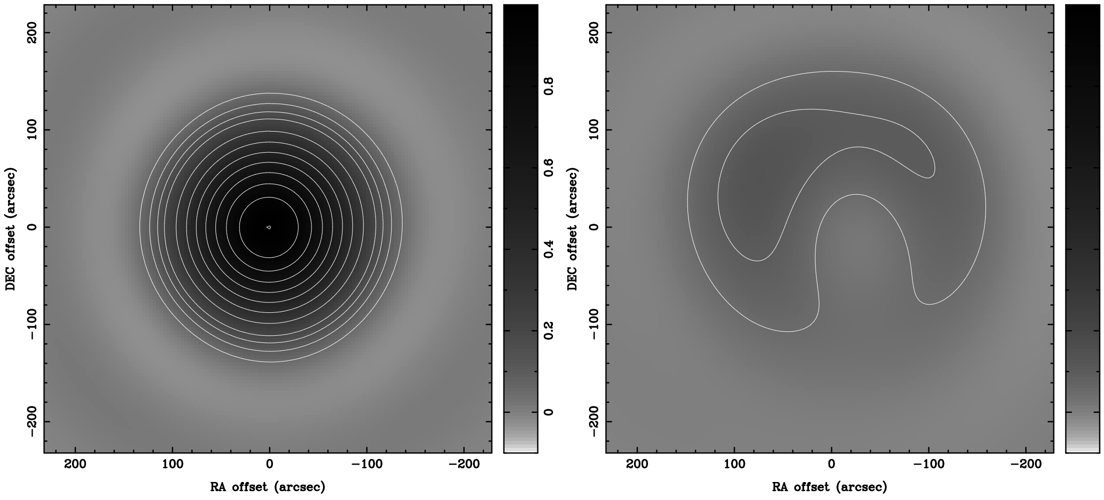

Figure 2.42 Similar to 2.32 but for antenna C11.

- **A suite of antenna specific voltage patterns to be used in cases were the ultimate image fidelity is needed.**

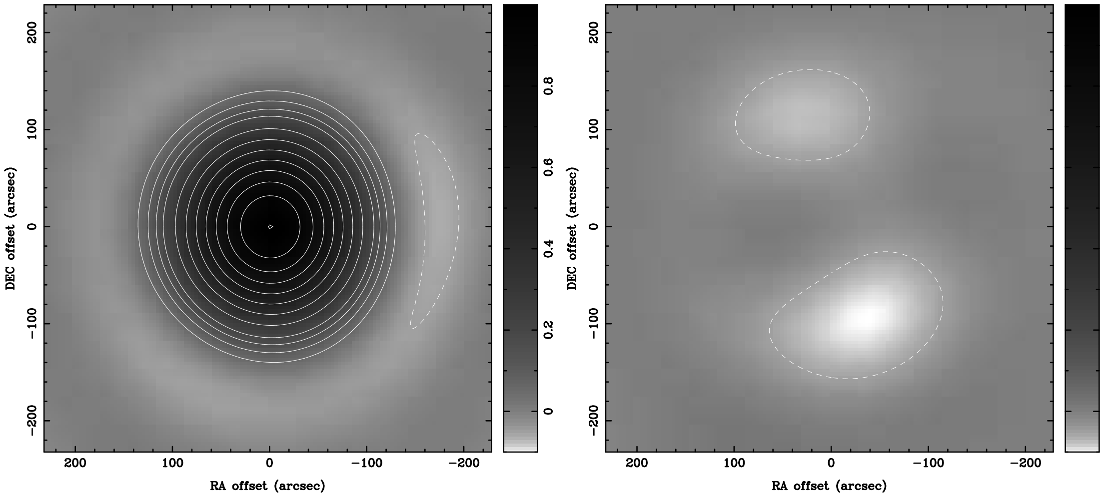

Figure 2.43 Similar to 2.32 but for antenna C12.

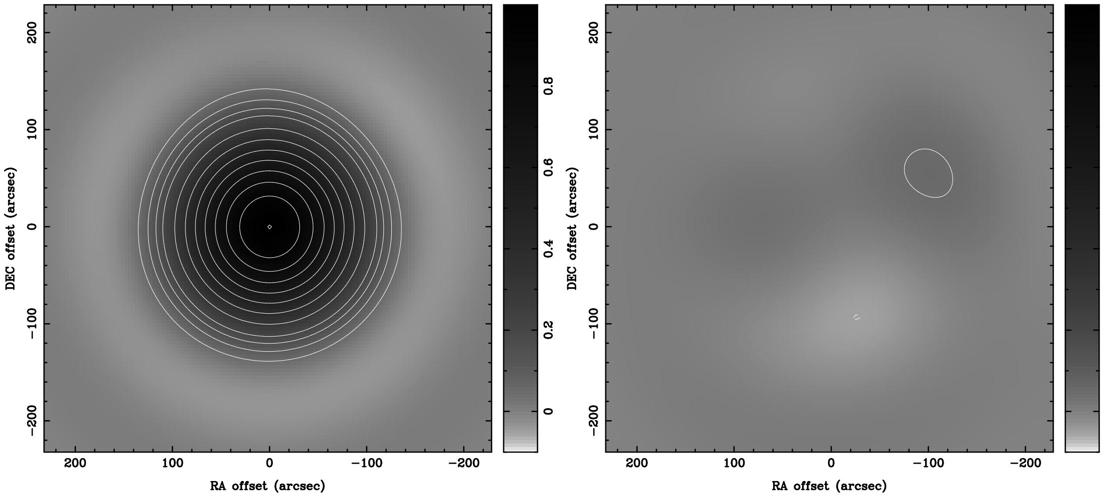

Figure 2.44 Similar to 2.32 but for antenna C13.

In these goals, I have succeeded. The width of the default model for the 6.1 m antenna and heterogeneous primary beams were significantly larger than the measured value and these values are now integrated into the default imaging program for

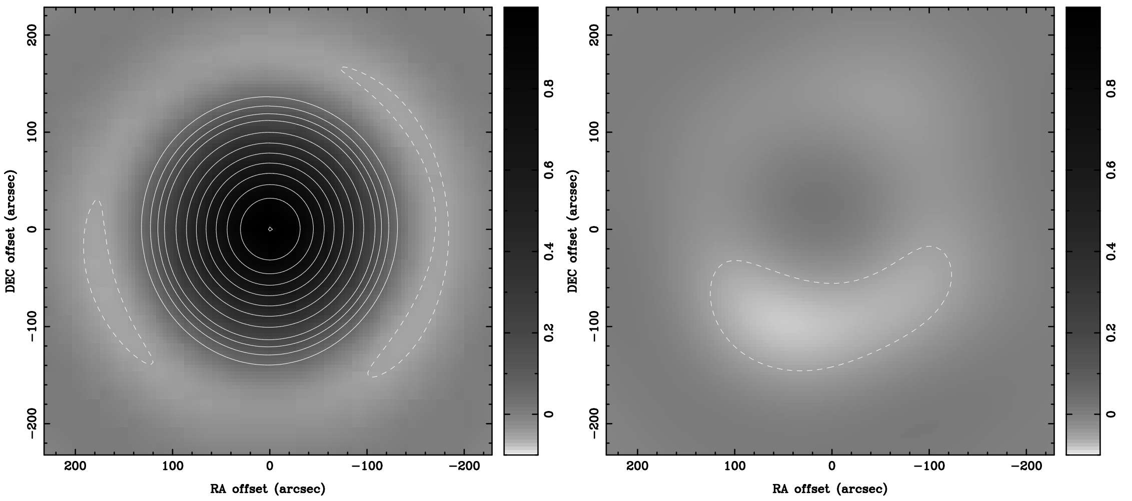

Figure 2.45 Similar to 2.32 but for antenna C14.

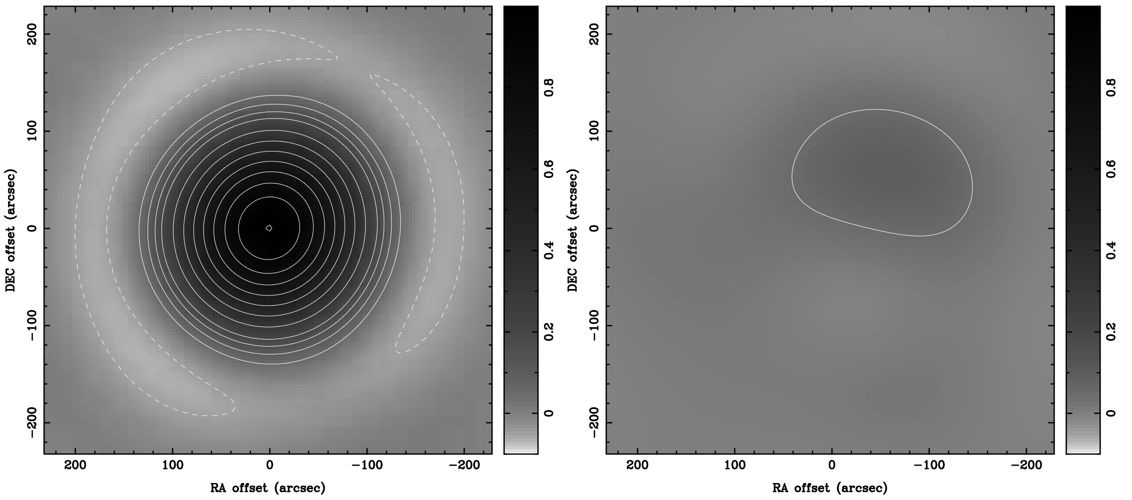

Figure 2.46 Similar to 2.32 but for antenna C15.

CARMA, MIRIAD. The symmetric, Gaussian model was found to be a reasonable approximation for the three CARMA primary beams but there are limitations which are effecting the current imaging process in noticeable ways. The 5%, or *cutoff*, point is uniformly narrower for the measured primary beams when compared to a best-fit Gaussian model. The deviations from the best-fit Gaussian range from 3 to 6" at that point. At the 1% level, which will become important with the inclusion of the 3.5 m, SZA antennas, the measured profiles are even more narrow. Given these 1% points will actually be multiplied up to 10% or more when combined with the 3.5 m antennas, a model must be provided. The profiles measured here can easily provide that model. *A fit to the profiles is provided in Appendix* **??**. Finally, I have provided an empirical suite of voltage patterns for each antenna to be used in cases were the highest dynamic range and image fidelity is required.

Bibliography

Cornwell, T. J., Holdaway, M. A., & Uson, J. M. 1993, A&A, 271, 697

Plambeck, R. L. 2008, private communication

Sault, R. J., Teuben, P. J., & Wright, M. C. H. 1995, ASPC, 77, 433

White, S. & Corder, S. A. 2007, CARMA Memo #40

Woody, D. P. 2008, private communication

Chapter 3

Applications: High-Resolution Imaging of the Young, Massive Stars NGC 7538-IRS1and NGC 7538S

Abstract

We present high-resolution (1″), Combined Array for Research in Millimeter-wave Astronomy (CARMA) images of the young, massive stars NGC 7538-IRS1and NGC 7538Sin HCO$^+$(1-0), ^{13}CO(1-0), C^{18}O(1-0), and 3 mm continuum emission. The continuum emission from NGC 7538Sis consistent with thermal emission from dust when compared with available multi-wavelength observations. The emission is well resolved and contains a large scale envelope with mass XX and extent XX. A more compact, torus-like structure, is evident with properties XXX and XXX. Continuum emission from NGC 7538-IRS1is brighter than expected from extrapolated, free-free, continuum emission at longer wavelengths indicating the presence of thermal emission from dust. The relative flux from 90 GHz and 110 GHz suggests that the emission is XXX. Continuum emission is also detected from NGC 7538 IRS2 and IRS3 with IRS2 exhibiting both diffuse and compact structures.

NGC 7538-IRS1shows definitive evidence of infall through self-absorption in HCO$^+$(1-0)with infall velocity of XX at the stellar position, falling off to XX several beam

---

widths away. The mass accretion rate is determined to be XX$M_\odot$ yr^{-1}. Both NGC 7538-IRS1and NGC 7538Sshow evidence of significant, collimated outflow which suggests the presence of a circumstellar disk. NGC 7538Sshows some signatures of rotation in C^{18}O(1-0)though there is still substantial confusion with outflow structures and the cloud. The outflow from NGC 7538-IRS1does not appear to be aligned with the direction of the ultra-compact HII region associated with NGC 7538-IRS1indicating the presence of multiple driving sources or rotation of the outflow axis.

3.1 Introduction

Historically in astrophyics, the creation of very massive stars presented a serious problem. Stars more massive than about XX$M_\odot$reach the main sequence before mass accertion terminates. These stars

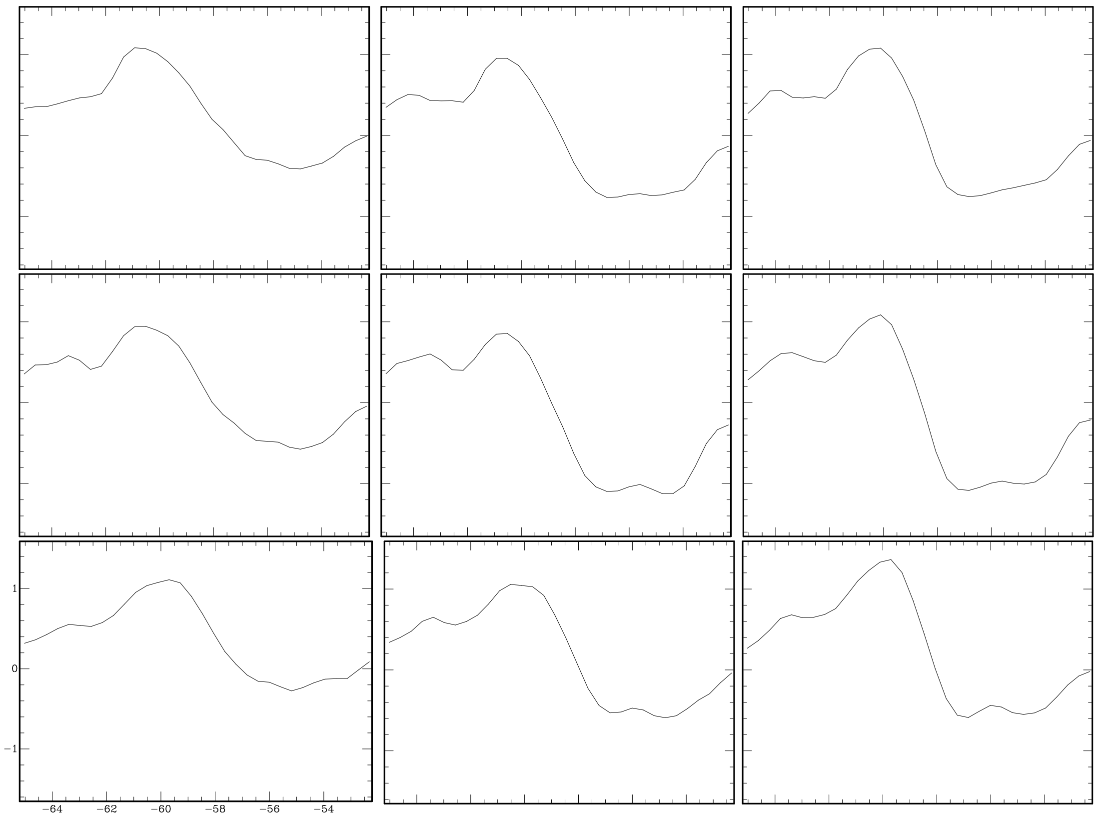

Figure 3.1 Inverse P-Cygni profile toward nine positions centered on NGC 7538-IRS1.

Bibliography